

## The Effect of Orographically Excited Gravity Wave Drag on the General Circulation of the Lower Stratosphere and Troposphere

N. A. MCFARLANE

*Canadian Climate Centre, Downsview, Ontario M3H 5T4*

(Manuscript received 28 August 1985, in final form 15 July 1986)

### ABSTRACT

The influence of large-scale momentum sinks, due to breaking of orographically excited gravity waves, on the Northern Hemisphere wintertime circulation of the troposphere and lower stratosphere is examined by introducing a simple wave drag parameterization into the Canadian Climate Centre general circulation model (GCM).

Results from GCM climate simulations are presented to show that the large-scale momentum sinks resulting from breaking gravity waves play an important role in determining the structure of the large-scale flow in the troposphere and lower stratosphere. It is argued that these results provide convincing evidence of the importance which must be attached to representing such wave drag effects in models designed for numerical weather prediction and general circulation studies.

### 1. Introduction

Gravity waves can be excited when stably stratified air flows over irregular terrain. Such waves may propagate freely to considerable altitudes before being significantly dissipated or absorbed. While orographic excitation is one of the more common sources of vertically propagating gravity waves they may also occur in association with a number of other processes such as the onset of shear instabilities and the rapid development of convective complexes and squall lines.

An important property of vertically propagating gravity waves is that they are able to transport momentum between their source regions and regions where they are dissipated or absorbed. The wave momentum flux convergence or divergence which occurs in association with dissipation or absorption may be of sufficient magnitude and horizontal extent to substantially modify the larger-scale mean flow. According to linear theory (Booker and Bretherton, 1967), wave absorption occurs near critical levels when the gradient Richardson number associated with the mean flow is substantially larger than 0.25. However, dynamical instabilities of the Kelvin-Helmholtz type and/or convective instabilities may occur in association with either the approach to a critical level or the tendency for vertically propagating waves to amplify with height due to the decrease in mean air density. The small-scale turbulent motions which develop in association with the onset of these instabilities may lead to wave dissipation with associated momentum flux convergence. The term "wave saturation" is now commonly used in reference to such dissipative effects. It is generally believed that momentum sources and sinks which arise

in association with gravity wave saturation are an essential ingredient of the large-scale circulation of the middle atmosphere.

Much of the recent work on gravity wave saturation has been stimulated by Lindzen's (1981) proposal of a simple parameterization of the effects of wave breaking associated with the onset of convective instability. That scheme is based on the assumption that just sufficient turbulent dissipation occurs in association with convective overturning to limit the growth with height of the gravity wave amplitude without otherwise substantially affecting its structure. Use of this saturation hypothesis in conjunction with the assumption that the mean flow varies slowly on spatial scales characteristic of the wave leads to a simple expression for the mean flow acceleration associated with wave breaking.

Recently a number of theoretical studies have appeared dealing with various aspects of the wave saturation process and other processes, such as wave transience and nonlinearity, which affect the way in which gravity waves interact with the mean flow. Modeling studies, such as that of Holton (1982), have demonstrated that the incorporation of momentum sources and sinks, due to gravity wave saturation, into zonally averaged models of the mesospheric circulation can lead to realistic simulations of the mean zonal flow structure. The review article by Fritts (1984) contains a summary of recent work on this subject.

Although the role of gravity wave saturation in the large-scale dynamics of the mesosphere has been studied extensively in recent years, much less attention has been paid to the effects of such processes on the general circulation of the stratosphere and troposphere. Lilly (1972) presented observational data to support the

contention that gravity wave momentum flux divergence associated with orographically excited waves may quite commonly occur in the upper troposphere and lower stratosphere and be of sufficient magnitude and horizontal extent to substantially affect the larger-scale flow in those regions.

Such stationary, nearly steady gravity wave systems with horizontal wavelengths of the order of several tens of kilometers occur commonly in mountainous regions. The principal features of a number of such wave events, observed in the Colorado Rocky Mountains, have been summarized by Lilly et al. (1982). The observational data presented by these authors indicate that typical wave systems have many of the features which would be expected on the basis of linear steady state wave theory. Observed wave momentum fluxes (averaged over horizontal areas of about  $10^5 \text{ km}^2$ ) are typically a few tenths of a Pascal in magnitude and extend throughout the troposphere. The observed wave structure is typically dominated by long (several tens of kilometers) nearly hydrostatic waves which commonly exhibit enhanced forward steepening of isentropic surfaces in the upper troposphere and lower stratosphere.

The appearance of such regions of enhanced steepening may be due in part to nonlinear effects of finite mountain heights. Enhanced intensities of clear air turbulence are often observed in such regions and may be associated with the occurrence of convective instabilities (Smith, 1977). The wave event documented by Lilly and Kennedy (1973) provides an interesting example in which all of the above features were present. More recent examples may be found in the studies by Brown (1983) and Hoinka (1984).

Although many of the basic features of observed mesoscale mountain waves can be described using linear steady state theory, it should be noted that theoretical and modeling studies have revealed a number of nonlinear and temporal effects which could be important in some circumstances. The effect of nonlinearity due to finite mountain heights on wave steepening has already been mentioned. This nonlinearity can also lead to enhancement of wave momentum fluxes and increased likelihood for the occurrence of convective instabilities in regions of enhanced steepening (Miles and Huppert, 1969; Smith, 1977; Lilly and Klemp, 1979).

A nonlinear resonant amplification effect, associated with the onset of convective instability, has been revealed in the recent modeling studies of Peltier and Clark (1979, 1983) and Durran and Klemp (1983). Although the physical mechanisms which lead to this effect are not yet well understood, it is likely that this amplification process plays an important role in the development of large-amplitude wave events with strong downslope winds such as those studied by Lilly and Zipser (1972), Lilly (1978), and Hoinka (1985).

The observational and theoretical studies just cited

reinforce the idea that the momentum flux divergence associated with mesoscale mountain waves may have a substantial impact on the larger-scale circulation of the troposphere and stratosphere. An additional reason for considering such effects is that many of the numerical models currently used for general circulation studies and weather forecasting have systematic deficiencies which may be ascribed to inadequate representation of the effects which unresolved orographic variations have on the simulated circulation.

An example of this is the well-known tendency for such models to develop excessively strong wintertime polar vortices in the stratosphere. Mahlman and Umscheid (1983) have commented on this tendency in the GFDL "SKYHI" model and suggested that its occurrence may be due to the combined effects of insufficient planetary wave activity in the lower stratosphere and the absence of momentum sources and sinks associated with unresolved gravity wave breaking. Recent studies with other large-scale models have documented similar deficiencies and provided evidence for both of these possibilities.

The effect of enhancing the dissipation acting on planetary-scale waves in the lower stratosphere has been studied by Boville (1984) using the NCAR Community Climate Model. These studies demonstrated that the tendency for development of an excessively strong stratospheric polar night vortex can be substantially reduced by this procedure. It was also found that certain deficiencies of the simulated circulation in the middle and lower troposphere were alleviated by enhancing planetary wave dissipation in the stratosphere. In particular the structure of simulated geopotential height fields was improved, notably in the regions of the climatological ridges over western North America and the eastern Atlantic. This effect was related to improvements in the simulated structure of the orographically forced stationary planetary waves.

Inadequate representation of the climatological features of geopotential height fields in the Northern Hemispheric wintertime circulation is a common defect of general circulation model simulations. This failing also leads to development of systematic errors in medium-range forecasts made with numerical weather prediction models. Wallace et al. (1983) have documented this effect for the ECMWF numerical weather prediction model and noted that a substantial part of the error is associated with the way in which the model responds to orographic forcing. It was found that locally enhancing the resolved orographic heights by an amount which is proportional to the variance associated with the unresolved part leads to significant reduction of systematic errors in medium-range forecasts.

Improvements due to the use of such "envelope orography" were of a similar nature to those found by Boville (1984). In this case, however, the improvement is due in large part to increased planetary wave amplitudes associated with the enhanced orographic forc-

ing. Blackmon (personal communication) has recently found that use of an envelope orography in the Community Climate Model produces similar effects and also reduces the cold bias in the polar night stratosphere. The planetary wave structure in the troposphere may also be sensitive to the effects of momentum sinks associated with unresolved motions in the stratosphere. Evidence for this was presented by the author and others (Boer et al., 1984a) in a paper which documents the Canadian Climate Centre general circulation model. In that paper some of the effects of using a simple parameterization of orographic wave drag in the GCM were discussed.

More recently, parameterization of orographic gravity wave drag effects has been replaced by one which makes use of the wave saturation concepts outlined by Linzen (1981) to represent wave drag effects and also makes use of a more realistic representation of sub-grid scale orographic variations which excite vertically propagating gravity waves. The purpose of the present paper is to discuss this wave drag parameterization and demonstrate how its use in the Canadian Climate Centre GCM alleviates many of the previously mentioned climate drift defects.

Section 2 is devoted to discussion of the wave drag parameterization. Section 3 is devoted to a brief description of the CCC general circulation model and an outline of the experiments which were performed with it. Results obtained for simulations both with and without gravity wave drag effects are presented and discussed in section 4. Finally, section 5 contains a summary of the main effects which are found to be associated with use of the wave drag parameterization.

## 2. Parameterization of wave drag effects in a GCM

### a. Basic theoretical considerations

Numerical models designed for general circulation studies or weather prediction typically have horizontal resolutions which are too coarse to permit explicit representation of the orographically excited gravity waves which have important wave drag effects. These effects must therefore be represented by means of a parameterization of the relevant wave properties in terms of the resolved flow. For a particular flow condition the wave response to orographic forcing may be very complicated, giving rise to a three-dimensional spectrum of waves having different orientations and amplitudes. This combination of waves may include both stationary and transient components. In order to develop a usable parameterization of wave drag effects on the larger-scale flow it is necessary to ignore much of this complexity.

The main aim of the present work is to determine whether including the typical wave drag effects in a GCM improves its ability to simulate the climate of the lower stratosphere and troposphere. To this end the wave drag parameterization used here is based on simple linear theory for steady monochromatic waves

with the momentum flux divergence due to wave breaking being represented in terms of a wave saturation hypothesis similar to that of Lindzen (1981).

The important wave properties can be summarized by considering the linear wave response associated with a steady, unidirectional, stably stratified mean flow over a corrugated boundary whose height deviations are of the form

$$Z = h \cos \mu x \quad (2.1)$$

where  $h$  is the amplitude of the orographic perturbation,  $\mu$  its wavenumber, and  $x$  is positive in the downstream direction. It is assumed that the typical horizontal wavelength ( $2\pi/\mu$ ) associated with the orographic variations is such that the flow is nearly in hydrostatic balance and the effects of Coriolis forces on the wave dynamics may be ignored. This implies that

$$\frac{f}{U} \ll \mu \ll \frac{N}{U} \quad (2.2)$$

where  $U$  and  $N$  are, respectively, representative values of the mean flow and Brunt-Väisälä frequency and  $f$  is the local Coriolis frequency.

Away from regions of dissipation associated with wave breaking and saturation processes, the linear wave dynamics are adequately represented, subject to the above assumptions, by the inviscid, adiabatic, steady state form of the anelastic equations (Ogura and Phillips, 1962) as follows:

$$\bar{U} \frac{\partial u}{\partial x} + w \frac{\partial \bar{U}}{\partial Z} = - \frac{\partial \Pi}{\partial x} \quad (2.3)$$

$$\frac{\partial \Pi}{\partial Z} = g \theta / \bar{\theta} \quad (2.4)$$

$$\frac{\partial u}{\partial x} + \frac{1}{\bar{\rho}} \frac{\partial}{\partial Z} (\bar{\rho} w) = 0 \quad (2.5)$$

$$\bar{U} \frac{\partial \theta}{\partial x} + w \frac{\partial \bar{\theta}}{\partial Z} = 0 \quad (2.6)$$

In these equations, mean quantities, denoted by overbars, are taken to be functions of height ( $Z$ ) only. Horizontal and vertical velocities are represented respectively by the symbols  $u$  and  $w$  while  $\theta$  denotes potential temperature and  $\Pi$  is defined in terms of the Exner function.

The mass continuity equation (2.5) and the thermodynamic equation (2.6) can be satisfied by defining  $u$ ,  $w$ , and  $\theta$  in terms of a streamline displacement function  $\psi(x, Z)$  as follows:

$$w = \bar{U} \frac{\partial \psi}{\partial x} \quad (2.7a)$$

$$u = - \frac{1}{\bar{\rho}} \frac{\partial}{\partial Z} (\bar{\rho} \bar{U} \psi) \quad (2.7b)$$

$$\theta = - \psi \frac{\partial \bar{\theta}}{\partial Z} \quad (2.7c)$$

The appropriate inviscid lower boundary condition is that the normal flow must vanish at those values of  $Z$  given by Eq. (2.1). In linearized form this condition is applied at  $Z = 0$  and is simply that the stream line displacement equals the orographic perturbation at that point, i.e.,

$$\psi(x, 0) = h \cos \mu x. \quad (2.8)$$

A radiation condition ensuring upward and downstream propagation of wave energy must also be applied.

Combining (2.7) with (2.3) and (2.4) gives the following equation for the stream line displacement function:

$$\frac{\partial}{\partial Z} \left[ \frac{\bar{U}^2}{\bar{\rho}} \frac{\partial}{\partial Z} (\bar{\rho} \psi) \right] + N^2 \psi = 0. \quad (2.9)$$

The squared Brunt-Väisälä frequency ( $N^2$ ) is defined in terms of the mean potential temperature in the form

$$N^2 = \frac{g}{\bar{\theta}} \frac{\partial \bar{\theta}}{\partial Z}. \quad (2.10)$$

This quantity is assumed to be positive definite everywhere.

An approximate analytical solution to Eq. (2.9) satisfying the stated boundary conditions can be obtained in circumstances such that vertical variations of the mean quantities ( $\bar{U}$ ,  $\bar{\rho}$ ,  $N^2$ ) occur on length scales which are longer than these which characterize the vertical variations of the streamline displacement function. In such circumstances, away from critical levels (where  $\bar{U} = 0$ ), a WKB type of approximation procedure consists in assuming a solution of the form

$$\psi(Z, x) = A(Z) \cos \left[ \mu x + \int_0^Z \phi(Z') dZ' \right] \quad (2.11)$$

where the amplitude,  $A$ , and phase function,  $\phi$ , are assumed to vary in the vertical on length scales characteristic of the mean flow. Substituting the form of  $\psi$  given by (2.11) into (2.9) and equating coefficients of corresponding trigonometric functions gives

$$(N^2/\bar{U}^2) - \phi^2 + O[(1/A)(d^2 A/dZ^2)] = 0 \quad (2.12)$$

$$2 \frac{dA}{dZ} + A \frac{d}{dZ} \left[ \frac{1}{(\phi \bar{\rho} \bar{U}^2)} \frac{d}{dZ} (\phi \bar{\rho} \bar{U}^2) \right] = 0 \quad (2.13)$$

The third term in Eq. (2.12) denotes a group of terms which are assumed to be negligible in the first approximation. With this assumption it is easily seen that an approximate solution satisfying boundary conditions is obtained by choosing

$$\phi = N/\bar{U} \quad (2.14)$$

$$A = h[(\bar{\rho}(0)N(0)\bar{U}(0)/(\bar{\rho}N\bar{U}))^{1/2}. \quad (2.15)$$

The approximations made here are based on the assumption that background quantities vary slowly enough in the vertical so that  $(\bar{U}/NH) < O(1)$  where

$H$  is the length scale associated with the most rapidly varying mean flow quantity. In regions where this condition fails wave reflection effects may occur. These effects may be sometimes important (Klemp and Lilly, 1975; Smith, 1977) but are ignored here.

The mean vertical momentum flux for the wave may be defined as

$$\tau = \frac{1}{L} \int_{-L/2}^{L/2} \bar{\rho} u w dx$$

where the length scale  $L$  encompasses at least one horizontal wavelength of the wave. The above approximate solution can be used to show that

$$\tau \approx -\frac{\mu h^2}{2} \bar{\rho}(0) N(0) \bar{U}(0). \quad (2.16)$$

This expression is independent of height, as expected, but is not valid in regions where wave dissipation processes are important.

#### b. Wave breaking and saturation

The approximate solution just obtained clearly fails at a critical level where the amplitude function becomes infinite. Well away from such a point, however, the wave amplitude may be large enough for nonlinear effects and saturation processes to become important. Of particular interest is the possibility that small-scale instabilities occur and lead to dissipation of the wave. One of the more important of these is associated with the onset of convective overturning. The locations of such regions can be found approximately by using the linear theory previously outlined to determine where the vertical gradient of the total (wave plus mean flow) potential temperature becomes negative. Using (2.7c) this condition can be stated in the following form:

$$\frac{\partial \bar{\theta}}{\partial Z} \left( 1 - \frac{\partial \psi}{\partial Z} \right) - \psi (\partial^2 \bar{\theta} / \partial Z^2) \leq 0.$$

The last term in this expression is usually negligible and, by assumption, the mean potential temperature increases with height in the region of interest. Thus, as a first approximation, convective instability will occur in regions where the vertical gradient in the streamline displacement exceeds unity. Using the approximate solution and associated scaling assumptions this condition can be expressed in the approximate form

$$-F(Z) \sin(\mu x + \phi) > 1 \quad (2.17)$$

where the quantity

$$F(Z) = \frac{Nh}{\bar{U}} \left[ \frac{\bar{\rho}(0)N(0)\bar{U}(0)}{\bar{\rho}N\bar{U}} \right]^{1/2} \quad (2.18)$$

is referred to as the local Froude number.

Equation (2.17) implies that convective instability may occur in regions where the local Froude number

exceeds unity. The onset of convective instability would lead to turbulent dissipation of wave energy. Lindzen (1981) and Holton (1982) assumed that the effects of this process may be simply represented by supposing that the turbulence leads to diffusive vertical heat and momentum transports which limit the wave amplitude. The eddy diffusivity associated with this process was assumed to be of such a magnitude as to prevent the amplitude of the wave from exceeding the critical value for the onset of convective instability.

To apply this saturation hypothesis in the present analysis, the solution given in Eq. (2.14) must be modified in such a way as to account for the effects of diffusive vertical transports acting on the wave. It will be assumed that the eddy diffusivity ( $K$ ) associated with this process is of such a magnitude that

$$[N^2/(\mu\bar{U}^3)]K \leq O(\bar{U}/NH). \quad (2.19)$$

When such is the case the main effects of the diffusive process can be taken into account by multiplying the approximate amplitude given in (2.15) by an exponential damping term leading to a modified approximate solution of the form

$$\psi = \psi_I \exp \left[ - \int_0^Z D(Z') dZ' \right] \quad (2.20)$$

where  $\psi_I$  is given by (2.11), (2.14) and (2.15) and

$$D(Z) = N^3 K / (\mu \bar{U}^4). \quad (2.21)$$

These modifications imply a modified form for the wave momentum flux. Using (2.19) and (2.20) it can be shown that

$$\tau = \tau(0) \exp \left[ -2 \int_0^Z D(Z') dZ' \right] \quad (2.22)$$

where  $\tau(0)$  is given by (2.16).

The saturation hypothesis is simply that  $D(Z)$  is of such a magnitude as to ensure that  $|\partial\psi/\partial Z|$  does not exceed unity. Equation (2.19) permits this condition to be expressed approximately as

$$F(Z) \exp \left[ - \int_0^Z D(Z') dZ' \right] \leq 1. \quad (2.23)$$

The implications of this condition are most easily illustrated by referring to Fig. 1 which shows schematically a possible vertical profile for  $F(Z)$ . In this figure  $F(Z)$  is less than unity in the region below the point  $Z_1$ . In this region convective instability does not occur so that  $D(Z)$  is zero. Between  $Z_1$  and  $Z_2$  the local Froude number exceeds unity and increases with height. Equation (2.23) can be satisfied by the choice

$$D(Z) = \frac{1}{F} \frac{dF}{dZ} \quad (2.24)$$

and this also implies that

$$\tau = \tau(0)/F^2 = -\frac{1}{2}(\bar{\rho}\mu\bar{U}^3/N). \quad (2.25)$$

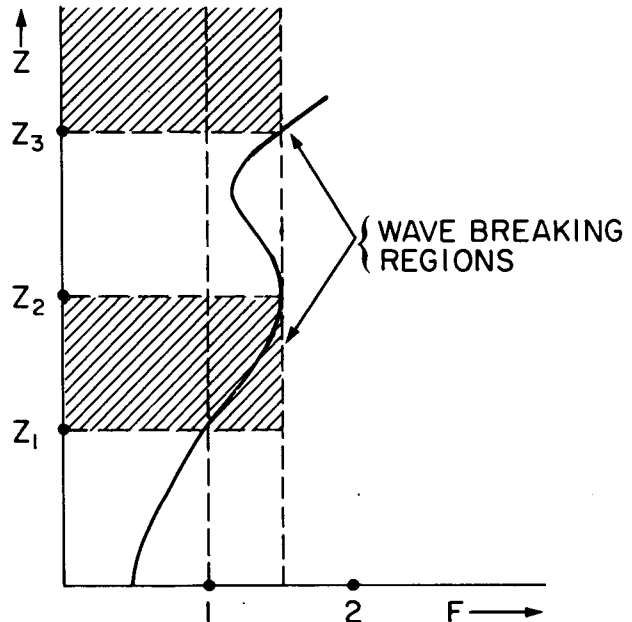


FIG. 1. Schematic vertical structure of the local Froude number illustrating regions of wave breaking and saturation.

Between  $Z_2$  and  $Z_3$  the wave amplitude has been sufficiently reduced by wave breaking in the region below so that convective instability does not occur even though the local Froude number exceeds unity. In this region condition (2.23) is clearly satisfied because, by virtue of (2.24),

$$\exp \left[ - \int_{Z_1}^{Z_2} D(Z) dZ \right] = 1/F(Z_2) \quad (2.26)$$

and hence the effective Froude number equation (2.23) is less than unity. Thus  $D(Z)$  vanishes at  $Z_2$  [by (2.24)] and remains zero in the region between  $Z_2$  and  $Z_3$ . Above  $Z_3$ , convective instability occurs again and  $D(Z)$  becomes nonzero to maintain a neutral (saturated) state.

The wave momentum flux decreases with height according to (2.25) in the wave saturation regions. Between these regions no wave dissipation due to breaking occurs and the wave momentum flux is (in the absence of other dissipative processes) independent of height. A simple way to represent the vertical variation is to include the damping factor in the definition of the wave amplitude so that the wave momentum flux has the form

$$\tau = \tau(0)(A^2\bar{\rho}N\bar{U})/[A^2(0)\bar{\rho}(0)N(0)\bar{U}(0)] \quad (2.27)$$

where  $A(Z)$  is such that the right-hand side of this equation is independent of height except in saturated regions where

$$A(Z) = \bar{U}/N. \quad (2.28)$$

This definition of  $A(Z)$  also ensures complete depletion of the wave at a critical level where  $\bar{U}(Z)$  vanishes. The implied mean flow change in these circumstances is given by

$$\partial \bar{U} / \partial t = -\frac{1}{\rho} \partial \tau / \partial Z = -\frac{\mu}{2} \frac{\bar{U}^3}{N} \text{Max}[d(\ln F^2)/dZ, 0]. \quad (2.29)$$

A similar equation has been presented by Holton (1982).

The vertical structure of the local Froude number in the troposphere and lower stratosphere is shown in Fig. 2 for typical midlatitude wintertime profiles of the mean flow and Brunt-Väisälä frequency. These profiles were constructed from zonally averaged climatological data taken from Newell et al. (1972). The Froude number profile shown in the figure is normalized to a value of unity at a reference level of 700 mb. Such a value would occur, for the given reference level wind

speed and Brunt-Väisälä frequency, in association with an orographic perturbation amplitude of 700 m. Mesoscale orographic variations of this magnitude are typical of regions with high rough mountains such as the Rockies.

The vertical structure of the local Froude number is strongly influenced by vertical variations in the flow speed. This is evident in Fig. 2 where it is seen that the effect of increasing wind speeds with height counteracts that of decreasing density to a sufficient degree to cause the local Froude number to decrease with height throughout most of the troposphere. The same effect is seen in the stratosphere above the 30 mb level. However, the combined effects of decreasing wind speed and air density cause the local Froude number to increase rapidly with height in the region above the tropospheric jet. For the profile shown, the simple wave saturation theory just outlined predicts wave breaking and momentum flux divergence in the region between 100 and 30 mb.

The foregoing discussion assumes that the local Froude number does not exceed unity in the lower troposphere. A number of complexities arise when the Froude number is order unity or greater near the surface. Of particular importance is the fact that the linearized lower boundary condition (2.9) is not appropriate in these circumstances. Smith (1977) and Lilly and Klemp (1979) have discussed a number of effects associated with this type of nonlinearity. Although its effects depend on the nature of the orographic perturbation, boundary condition nonlinearity typically suppresses wave steepening and the tendency for convective overturning near the surface while enhancing these effects in preferred regions aloft. Smith has illustrated how this effect, combined with the typical wintertime vertical structure of the local Froude number, suppresses the tendency for occurrence of convective instability in the troposphere while enhancing it in the lower stratosphere.

The previously noted studies have been based on the idealization of spatially two-dimensional flow. In reality the flow is always three-dimensional. An important consequence of this is that air near the surface can tend to flow around rather than over obstacles. Such orographic blocking effects are also likely to become important when the local Froude number is order unity or greater near the surface since, in this circumstance, the kinetic energy of the incoming air is less than the potential energy barrier which must be overcome to permit air parcels to surmount orographic obstacles.

Examples of this effect have been found in laboratory studies of stably stratified fluid flow over surface-mounted obstacles (Snyder et al., 1985). It has been found that the fluid which flows over the obstacle is confined to a region whose depth is  $O(h/F)$  where  $h$  is the maximum height of the obstacle. Since gravity wave excitation is associated with flow over, rather than

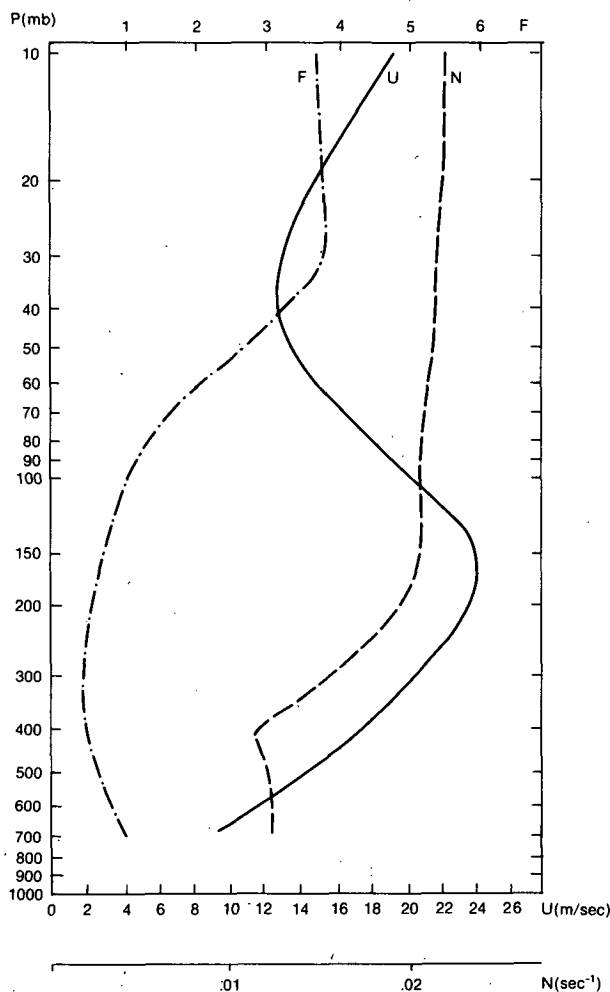


FIG. 2. Vertical structure of the local Froude number for typical midlatitude winter flow conditions.

around, orographic perturbations, it may be that this blocking effect would tend to limit both wave amplitudes and wave drag by reducing the effective obstacle heights. Lilly et al. have noted that blocking effects of this sort occur quite commonly in association with large amplitude mountain waves.

In reality, of course, there may be a complicated interplay between the effects of blocking, boundary condition nonlinearity, and effects due to other processes such as those associated with boundary layer turbulence. In any event the fact that both boundary condition nonlinearity and blocking effects may limit wave steepness in the lower troposphere does provide some justification (in addition to that provided by the limited amount of available observational data) for assuming that most of the wave momentum flux divergence associated with wave breaking is likely to be confined to the region above the lowest minimum in the local Froude number. This assumption is certainly not appropriate in circumstances where nonlinear resonant amplification (Peltier and Clark, 1979) occurs. In what follows this effect is ignored because it is not yet well understood and probably occurs sporadically. This is discussed further in section 5.

### c. Representation of wave drag effects in the GCM

In the AES spectral general circulation model the effects of such physical processes as radiative heating, latent heat release, and subgrid-scale vertical transfers are determined using local representations of GCM variables on a global grid with points distributed so as to permit implementation of the spectral transform technique (Orzag, 1970; Machenhauer and Rasmussen, 1972). The results of computations on this "Gaussian" grid are then transformed to provide tendencies in the spectral domain. This procedure is now standard practice in spectral modeling and is used here for wave drag effects as well. For this purpose it is assumed that the mean flow conditions can be defined using local values of GCM variables.

The wave momentum flux in the lower troposphere is assumed to act opposite to the mean flow at a specified reference level near the surface. Denoting large-scale flow conditions at that level by a zero subscript, the wave momentum flux there is defined as

$$\tau_0 = -\left(E \frac{\mu_e}{2} h_e^2\right) \rho_0 N_0 V_0 \quad (2.30)$$

where  $\mu_e$  and  $h_e$  are representative values of horizontal wavenumber and amplitude for a typical wave and  $E$  is an efficiency factor which is taken to be less than unity. These wave parameters are specified empirically on the basis of information obtained from mesoscale orographic height data and tuning experiments carried out with the GCM.

For simplicity, the effects of subgrid-scale orography in determining a preferred orientation for the wave

momentum flux have been ignored. In principle, such effects could be taken into account, for example, by making the efficiency factor a function of the angle between the reference level mean flow and the dominant ridge orientation in a given grid square.

In line with the saturation concept, the wave momentum flux is taken to be independent of height except in regions where wave breaking can occur. In such regions the wave amplitude is limited to the saturation value. Analogous to (2.27) the wave momentum flux vector is of the form

$$\tau(Z) = \tau_0 [A(Z)/h_e]^2 (\rho N U) / (\rho_0 N_0 U_0) \quad (2.31)$$

where  $A(Z)$  is the local wave amplitude. The wind speed  $U(Z)$  corresponds to that component of the flow which is parallel to that at the reference level, i.e.,

$$U = \mathbf{V} \cdot \mathbf{V}_0 / |\mathbf{V}_0|. \quad (2.32)$$

At any model level above the reference level  $A(Z)$  is first estimated in terms of the amplitude at the next lower level so as to maintain a constant momentum flux. This value is then constrained so as to ensure that it does not exceed the critical value for convective overturning, i.e.,

$$A(Z) \leq (U/N) F_c \quad (2.33)$$

where  $F_c$  is a critical Froude number. For a linear monochromatic wave this value is near unity as indicated in subsection 2b. In general the wave response will not be monochromatic. In such circumstances the effects of wave superposition and nonlinearity may cause convective instability to occur at smaller amplitudes than for a single wave. This is so, for example, in the case of gravity waves excited in flow over an isolated ridge (Lilly and Klemp, 1979). In addition, wave dissipation may result from other processes, of course, such as the occurrence of shear instabilities of the Kelvin-Helmholtz type.

These considerations suggest that  $F_c$  and any point is probably a function both of the underlying terrain structure and local mean flow conditions. In order to retain maximum simplicity, however, a single fixed value of  $F_c$  is used here.

The wave amplitude at the reference level is defined in terms of a measure of the subgrid-scale orographic variance but constrained so that the local Froude number does not exceed the critical value ( $F_c$ ). This constraint is introduced to account crudely for the effects of blocking. The chosen representation is

$$h_e = \min(2S_d, F_c U_0 / N_0) \quad (2.34)$$

where  $S_d$  is the standard deviation associated with that part of the subgrid scale orography which is most likely to give rise to vertically propagating gravity waves. The product  $(E\mu_e/2)$  is given a fixed value and is regarded as a tunable parameter.

The version of the CCC spectral GCM used in the present study utilizes a set of spherical harmonics tri-

angularly truncated at 20 waves. The large-scale orography used in the model contains only these spherical harmonic components. Thus, in low and middle latitudes, wavelengths less than about 1200 km are not resolved in the model. However, the orographically excited gravity waves of interest here have wavelengths which are short enough so that Coriolis effects can be ignored; they are substantially less than about 500 km in middle latitudes. Thus, it is appropriate to define  $S_d^2$  in terms of the variance about a mean orography which includes scales of variation down to about 500 km.

The U.S. Navy high-resolution dataset used for this purpose contains information on mean orographic elevations on a global latitude-longitude grid with a resolution of 10 min of arc. Using this data, a field of mean elevation on a  $1.8^\circ$  (200 long  $\times$  100 lat) grid was constructed by simply averaging together values from all of the high resolution grid "squares" contained in a given square of the coarser grid. The variance for about this mean field was found at the same time by averaging together the squared deviations from the coarser grid mean in each  $1.8^\circ$  grid square.

This variance field was then interpolated to a slightly coarser (192 long  $\times$  96 lat) Gaussian grid, transformed into spherical harmonics, truncated, and transformed back onto the coarser (64 long  $\times$  32 lat) Gaussian grid used in the GCM. All negative values, and nonzero values over oceanic points, which may have resulted from the interpolation and transformation process, are set to zero before using this spectrally smoothed variance field in the wave drag parameterization. The associated twice standard deviation field ( $2S_d$ ) is displayed in Fig. 3.

In practical application the wave drag parameterization is implemented by using (2.32) to define the stress at model levels and the implied mean flow acceleration is obtained by finite differencing. A semi-implicit time stepping scheme is used in conjunction with this procedure, details of which are given in the Appendix.

It should be noted here that the uppermost model level is treated differently from the others. It is commonly assumed in general circulation and NWP models that the dependent variables defined at this level represent mass weighted mean values for all of the atmosphere which remains above the interface between the uppermost two model layers. Since the saturation hypothesis implies that gravity waves must be completely dissipated within the atmosphere this assumption implies that the wave momentum flux must vanish at the top of the model. However, orographically excited gravity waves which reach the middle stratosphere can often propagate upward to mesospheric heights without undergoing further dissipation due to wave breaking.

At mesospheric heights the waves do break and provide a local wave drag force on the large-scale flow. As discussed by Holton (1982) this force is an important part of the momentum budget at these heights since it nearly balances the Coriolis torque due to the mean meridional circulation which, in turn, is locally forced by radiative heating.

In the CCC model this part of the atmosphere is not resolved and, in particular, the radiative heating in the model is determined in such a way that all radiative flux divergence (convergence) is explicitly ignored above the uppermost model level. Hence, for consis-

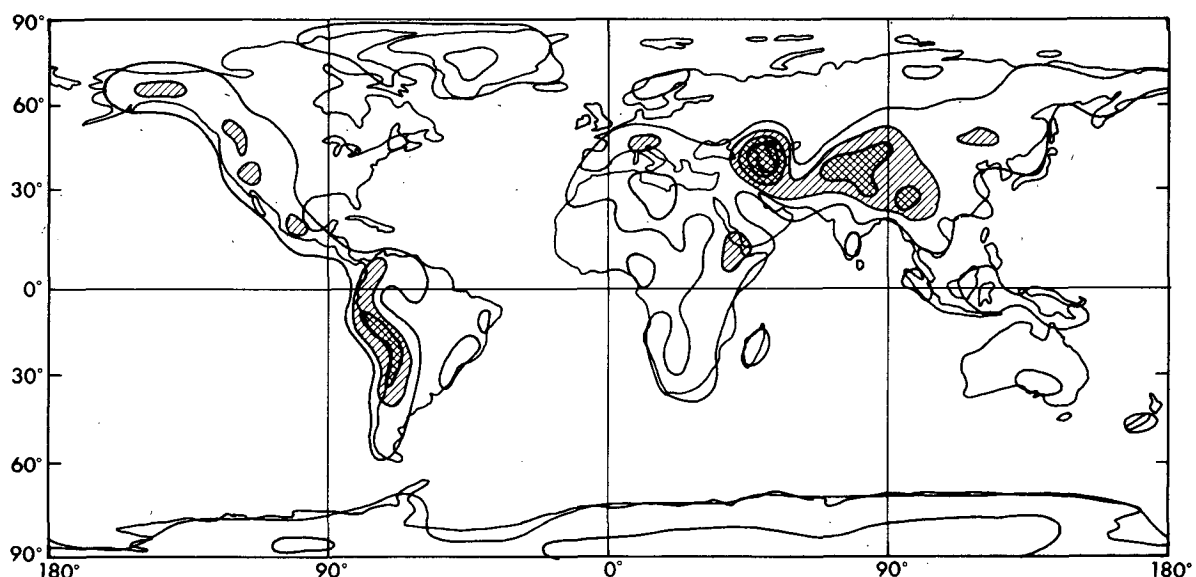


FIG. 3. Smoothed subgrid-scale orographic standard deviation field. Contours are of twice the standard deviation. The lowest value contoured is 250 m and the contour interval is 50 m. Regions with values in excess of 750 m are hatched; cross-hatched regions exceed 1250 m.



tency, the gravity wave momentum flux divergence is also ignored in that region. This amounts to allowing wave energy to escape through the top of the model in some circumstances.

### 3. GCM experiments

The CCC spectral general circulation model has been documented in detail by Boer et al. (1984a) and only a brief description of the model is presented here.

The model is based on the primitive equations of motion written in terms of vorticity and divergence. The remaining prognostic variables are temperature, dewpoint depression, and surface pressure. The assumption of hydrostatic balance enables use of the normalized pressure coordinate system (Phillips, 1957) in which vertical structure is represented in terms of the variable  $\sigma = p/p_s$  where  $p_s$  is surface pressure.

Standard second-order, accurate, finite difference procedures are used for vertical discretization in the model. In the version used here, prognostic variables are defined at ten distinct levels in the vertical with thermodynamic variables (temperature, dew point depression) being defined on levels which are staggered with respect to those used for vorticity, divergence, and geopotential height. Table 1 summarizes the leveling scheme.

The standard model physics package contains a relatively complete representation of the processes governing the hydrological cycle, small-scale turbulent

transfers in the boundary layer and the free atmosphere, and heating (cooling) due to solar and infrared radiation. Both diurnal and annual cycles are included in the representation of solar radiative forcing.

A representative climatology for this model was documented by Boer et al. (1984b). The earlier wave drag parameterization discussed in Boer et al. (1984a) was used in the model to establish this representative climatology. Since publication of these papers, the computer code was modified to permit more efficient running of the model at higher horizontal resolutions.

While this was being done, parts of the radiative heating code were changed to correct inaccuracies in the calculations. It is beyond the scope of this paper to discuss these changes in detail. It is sufficient to note that they mainly affect the upper part of the model and have reduced the tendency for rapid development of an excessively cold stratospheric polar night vortex.

There is, however, a tendency for development of unrealistically strong winds near the top of the model, particularly in the Southern Hemisphere during the polar night. Occasionally the flow in that region becomes strong enough to cause the onset of computational instability for the time-step increment normally used in the model (30 min). This problem occurs more frequently with higher horizontal resolutions than that employed in the present study.

In order to control this tendency a weak Rayleigh frictional damping was introduced at the top level of the model. The damping time used is generally 75 days but may be larger when kinetic energy dissipation due to wave drag is also present. In such cases the time scale is locally increased so as to ensure that the total dissipation rate due to the combination of Rayleigh friction and wave drag does not exceed that due to the larger of the two dissipation rates.

Experiments using this weak Rayleigh damping have led to the conclusion that substantial sensitivity to this process does not extend below the uppermost two model levels, at least for the time periods considered in the present study (simulations of 120 days). This conclusion may not hold for long simulations with fixed solar forcing such as those discussed by Boville (1984). As mentioned before, the CCC model is usually run with both diurnal and annual cycles in the solar forcing.

The response to the wave drag parameterization discussed in the preceding sections is illustrated by presenting selected results from two distinct GCM simulations of the Northern Hemisphere winter (December through February) climate. Each of these simulations was started from identical initial conditions (obtained from a time period on 1 November of an earlier model run which had already been carried through one annual cycle). In each case results presented are time averages over the last 3 months of a 4-month (November–February) simulation.

The control simulation (CONTROL) was carried out without any form of wave drag parameterization in the

TABLE 1. The vertical leveling scheme in the CCC general circulation model. Symbols: ( $\sigma$ ), normalized pressure velocity; ( $\zeta$ ), relative vorticity; ( $D$ ), horizontal divergence; ( $T$ ), temperature; ( $S$ ), dew point depression.

Variable	Level	$\sigma$
$\sigma = 0$	0	0
$\zeta, D, \phi$	1	0.010
$T, S, \sigma$	1.5	0.018
$\zeta, D, \phi$	2	0.032
$T, S, \sigma$	2.5	0.050
$\zeta, D, \phi$	3	0.080
$T, S, \sigma$	3.5	0.110
$\zeta, D, \phi$	4	0.150
$T, S, \sigma$	4.5	0.188
$\zeta, D, \phi$	5	0.235
$T, S, \sigma$	5.5	0.291
$\zeta, D, \phi$	6	0.360
$T, S, \sigma$	6.5	0.445
$\zeta, D, \phi$	7	0.550
$T, S, \sigma$	7.5	0.642
$\zeta, D, \phi$	8	0.750
$T, S, \sigma$	8.5	0.812
$\zeta, D, \phi$	9	0.880
$T, S, \sigma$	9.5	0.924
$\zeta, D, \phi$	10	0.970
$T, S, \sigma$	10.5	0.985
$\sigma = 0$	11	1.00

model. In the wave drag experiment (WD) the reference level was taken to coincide with the top of the lowest model layer and the *tunable* parameters were given the following values:

$$F_c^2 = 0.5 \quad (3.1a)$$

$$E\mu e/2 = 8 \times 10^{-6} \text{ m}^{-1}. \quad (3.1b)$$

As mentioned before, in reality these parameters vary with location and mean flow conditions. The fixed values used here for simplicity were chosen on the basis of results from several independent test simulations.

An additional wave drag experiment (WDH) was carried out to test sensitivity to vertical resolution in the region where the most pronounced wave drag effects occur.

#### 4. Results

The deceleration effects of parameterized wave drag are felt directly by the large-scale flow in the GCM. Dynamical processes, such as geostrophic adjustment, spread this direct influence to other large-scale fields such as temperature, surface pressure, and geopotential height.

The main features of the response of the flow field to parameterized wave drag are illustrated by comparing time and zonally averaged cross sections of westerly wind fields for the two experiments. Indirect effects on tropospheric pressure and geopotential height fields are demonstrated by examination of time averaged mean

sea level pressure and 500 mb geopotential height simulations. As mentioned in section 3 the time averaging period is the last 3 months (December–February) of the simulations.

##### a. Zonal winds and temperatures

Cross sections of zonally averaged observed climatological westerly wind and temperature fields are shown in Figs. 4 and 5, respectively. These figures are presented first to provide a reference for comparing the GCM simulations.

The corresponding fields for the CONTROL simulation are shown in Figs. 6 and 7, respectively. Comparison of Figs. 6 and 4 reveals several features of the zonal flow field which are in poor agreement with the observed climatological field. These are most prominent in the upper troposphere and lower stratosphere.

Although the magnitude of the zonal wind maximum in the polar night is in reasonable accord with climatology, this feature is positioned too far northward by about  $10^\circ$  of latitude. The polar night jet is too narrowly confined to high latitudes. The midlatitude tropospheric jet maximum in the Northern Hemisphere is both too large and too far northward. Moreover the zonal wind minimum between this feature and the polar night jet is poorly simulated. Comparison of Figs. 5 and 7 shows that the polar night region of the lower stratosphere is too cold in the CONTROL simulation. The presence of westerly winds in the CONTROL simulation in the Southern Hemisphere

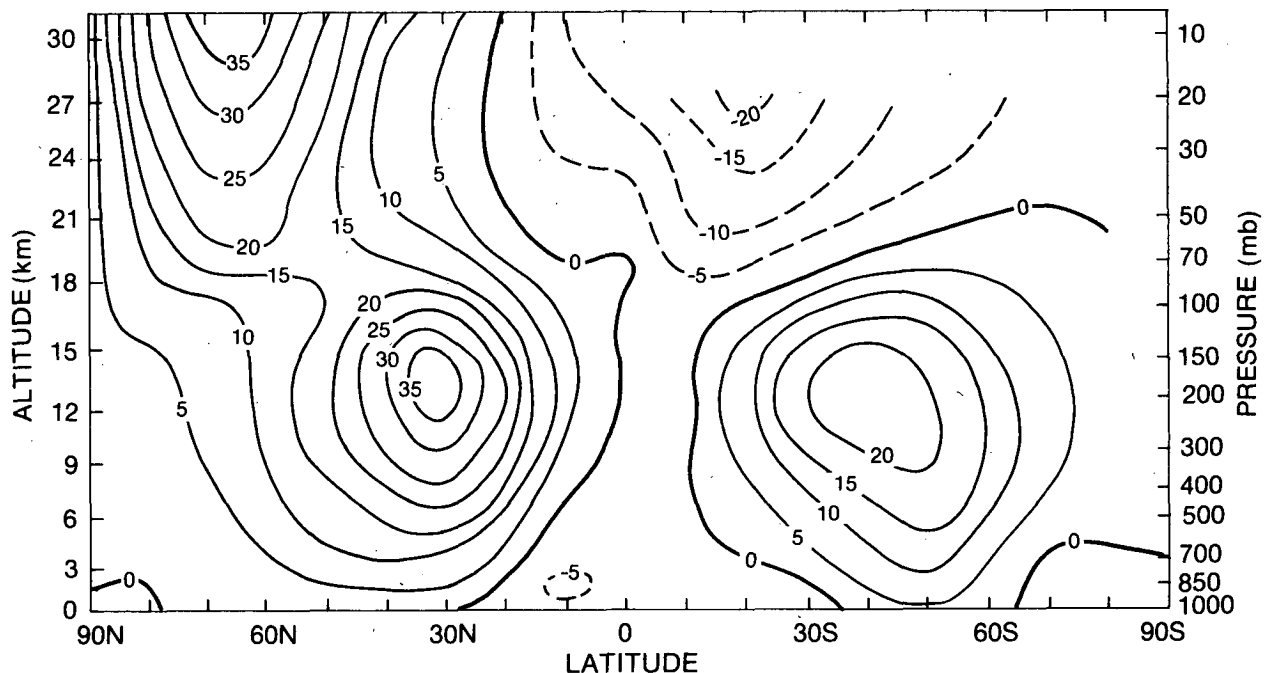


FIG. 4. Observed mean zonal winds for December through February (after Newell et al., 1972). Units:  $\text{m s}^{-1}$ . Contours every  $5 \text{ m s}^{-1}$ .

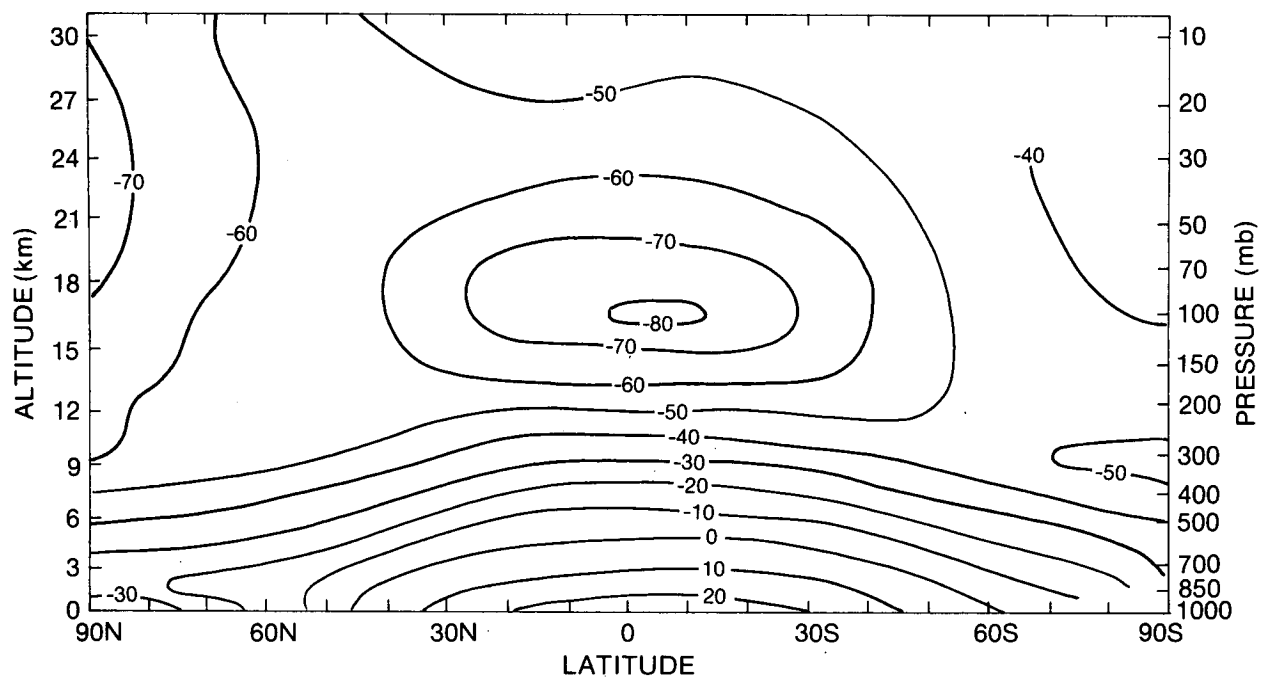


FIG. 5. Observed zonal mean temperature for December through February (after Newell et al.). Units: degrees Celsius.

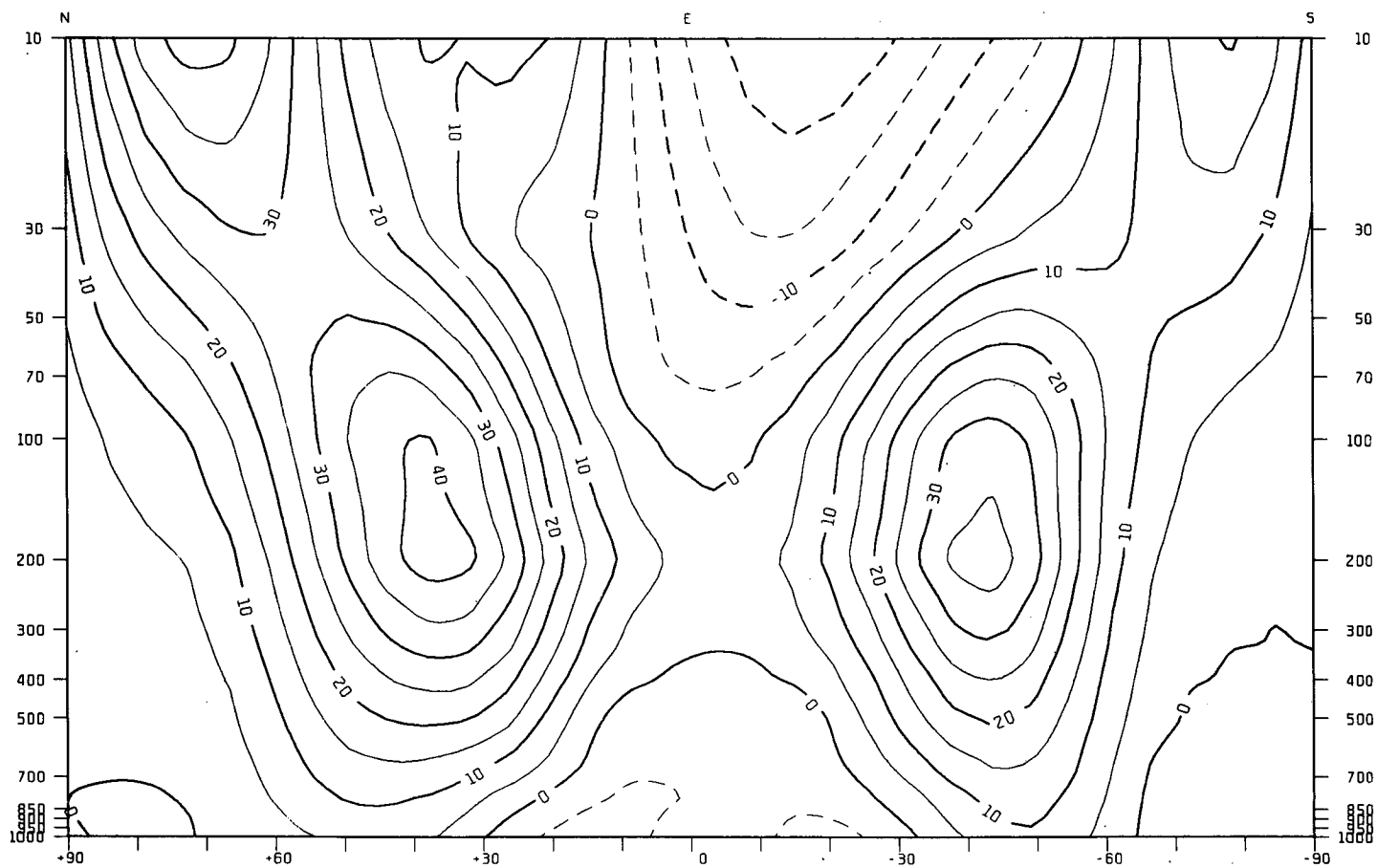


FIG. 6. Mean zonal winds for the control simulation.

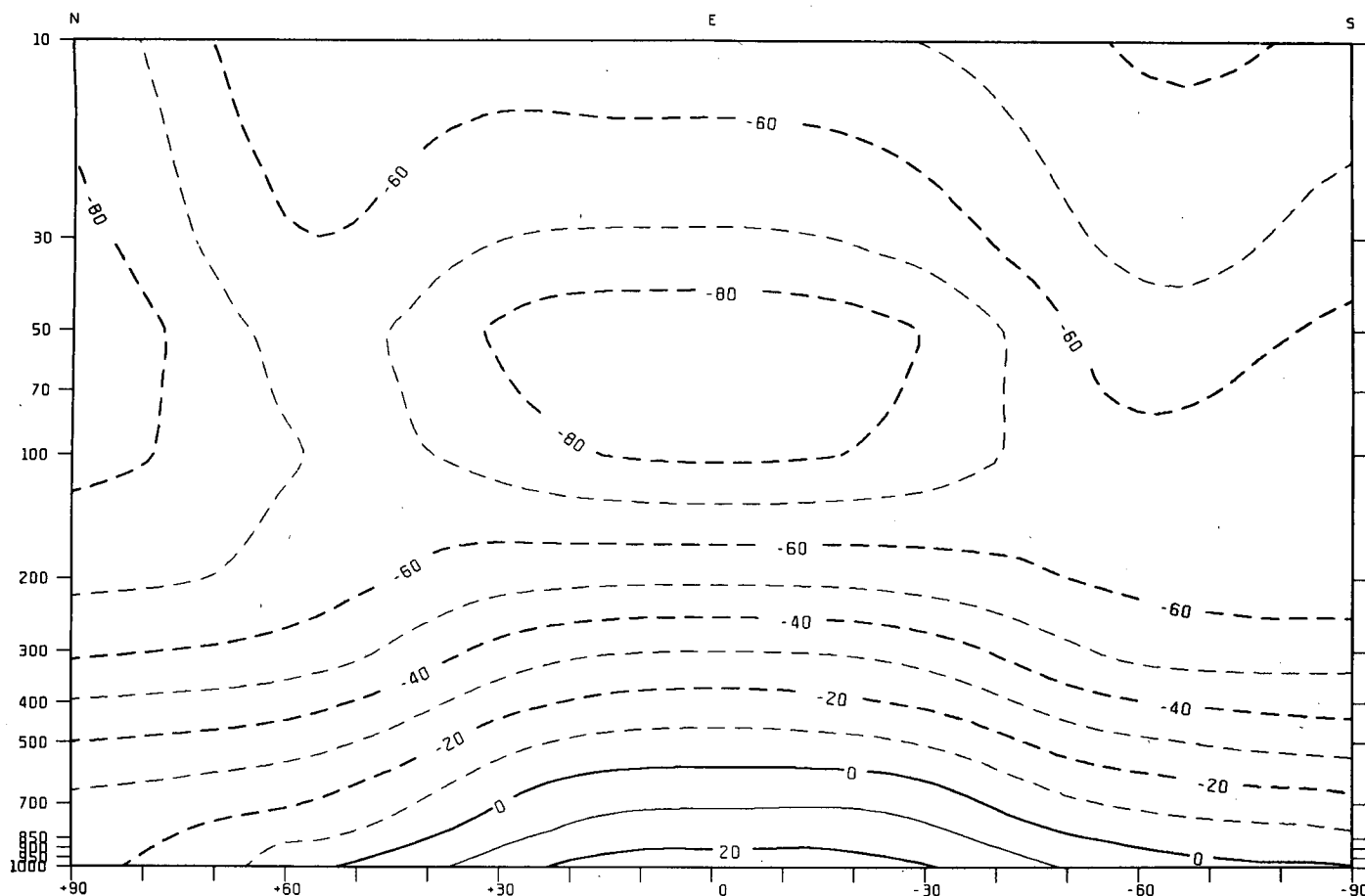


FIG. 7. Zonal mean temperatures for the control simulation.

stratosphere is an unphysical feature which may, in part, be associated with an inadequate response to solar radiative heating in that region.

The zonal-averaged westerly wind and temperature fields for the WD experiment are shown in Figs. 8 and 9. The most remarkable effect of wave drag on the mean zonal flow in the Northern Hemisphere is the substantial reduction of wind speeds in and above the tropospheric jet. Comparison of Figs. 6 and 8 illustrates quite clearly how introduction of the wave drag parameterization has resulted in development of a sharper separation between the polar night jet and the mid-latitude tropospheric jet.

The wave drag parameterization did not result in a significant change in the strength or position of the polar night jet. However, this feature is somewhat broader in latitudinal extent in the wave drag simulation. Thus the overall effect of the wave drag parameterization is to improve the simulated zonal flow structure.

Figure 10 depicts the difference between the CONTROL and WD simulations of the mean zonal flow. Not all of the features depicted in this figure can be

directly ascribed to the impact of the gravity wave drag parameterization. Long simulations of several annual cycles' duration exhibit a degree of interannual variability which is not dissimilar to that of the atmosphere. Moreover, two simulations of the same seasonal time period, if started with different initial conditions, may exhibit zonal wind differences of several meters per second in regions of high internal variability.

However, in Fig. 10 the large (negative) difference maximum centered near 60°N is a significant and direct result of the wave drag parameterization. The location of this feature corresponds closely with the region in which the most pronounced deceleration of zonal winds due to wave drag occurs. This is illustrated in Fig. 11 which depicts the time and zonally averaged westerly wind deceleration due to wave drag. The corresponding zonal mean meridional flow deceleration is shown in Fig. 12.

Of course it must be remembered that wave drag effects are determined locally in the model and confined to regions where there is substantial subgrid-scale orographic variance. More will be said about this in subsection (c). The zonally averaged values shown in these

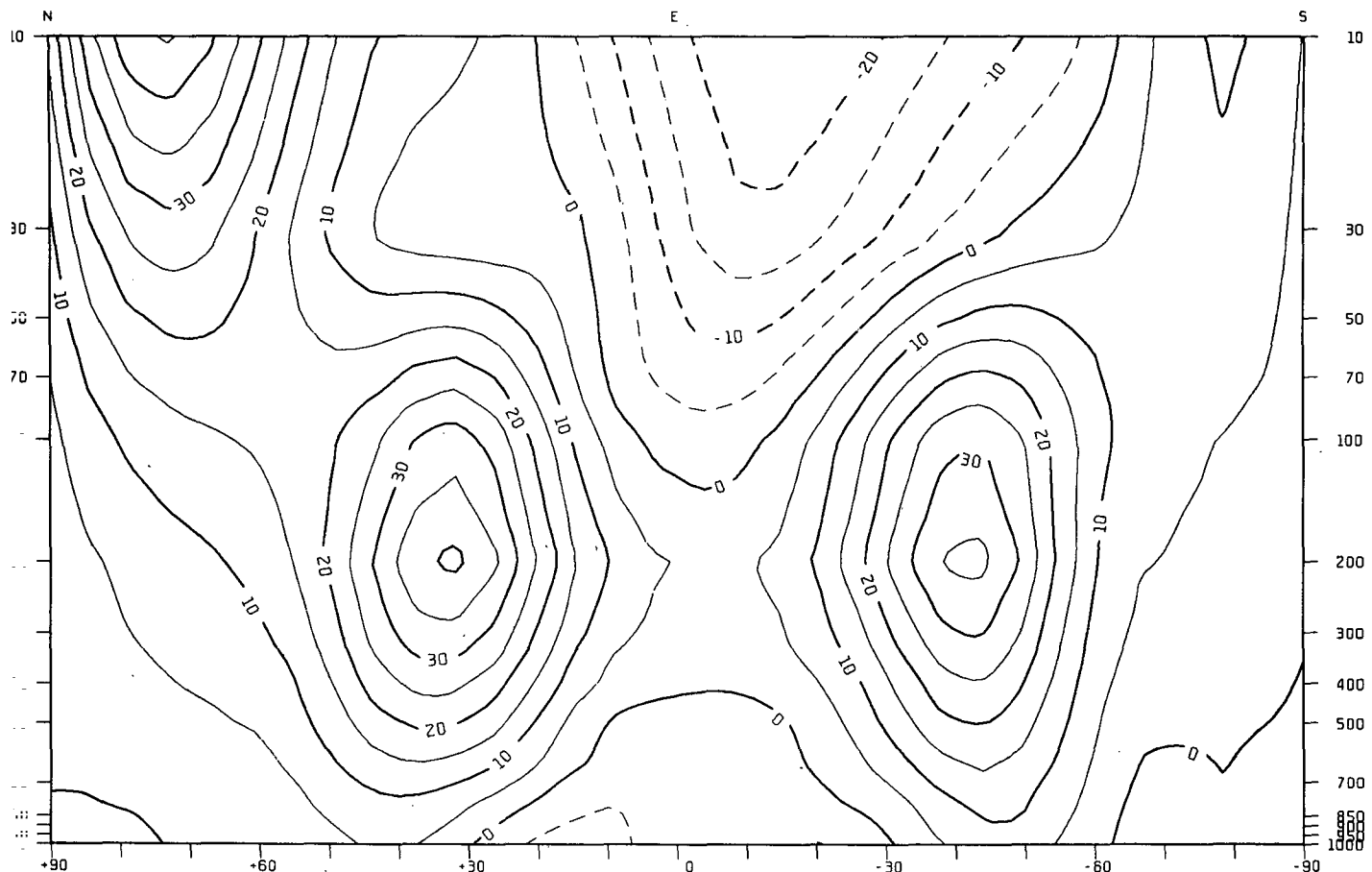


FIG. 8. As in Fig. 6, except for WD.

figures are substantially smaller in magnitude than those which may occur locally in regions of high rough terrain.

Figure 13 depicts the zonal mean temperature difference between the CONTROL and WD experiments. The warmer region, in the wave drag experiment, centered near 70°N and 100 mb is consistent with the reduction in vertical wind shear equatorward of that region. Thus, this feature appears to be a dynamical consequence of the imposition of wave drag.

Both the zonal wind and temperature difference fields show a more complicated structure in the upper part of the model, generally above 50 mb. These difference structures must be viewed in light of the fact that the circulation in that entire region is represented, in the GCM, by prognostic variables defined at the uppermost two model levels. Apart from the fact that the vertical resolution in this region is rather coarse there is a possibility that simulations may be contaminated to some extent by spurious numerical effects associated with application of the upper boundary condition. This condition is, formally, that the nor-

malized pressure velocity ( $\sigma$ ) vanishes at the top of the atmosphere ( $\sigma = 0$ ). In practice, however, the effects of coarse vertical resolution and associated inaccuracies in finite difference approximations are likely to be such that the effective top of the model atmosphere is a finite distance above the uppermost model level. In such circumstances a possible source of contamination may be associated with spurious reflection of upward propagating planetary waves. In general it is difficult to determine the extent to which a problem of this sort may significantly affect the quality of GCM simulations in the stratosphere.

Another possible source of error may be associated with representation of the effects of radiative heating in the upper levels of the GCM. Ramanathan et al. (1983) have demonstrated that simulations of the lower stratospheric circulation are sensitive to the way in which these processes are represented in the model. Experimentation with the CCC model has also revealed that the simulated circulation in the upper part of the model is sensitive to the radiative heating representation.

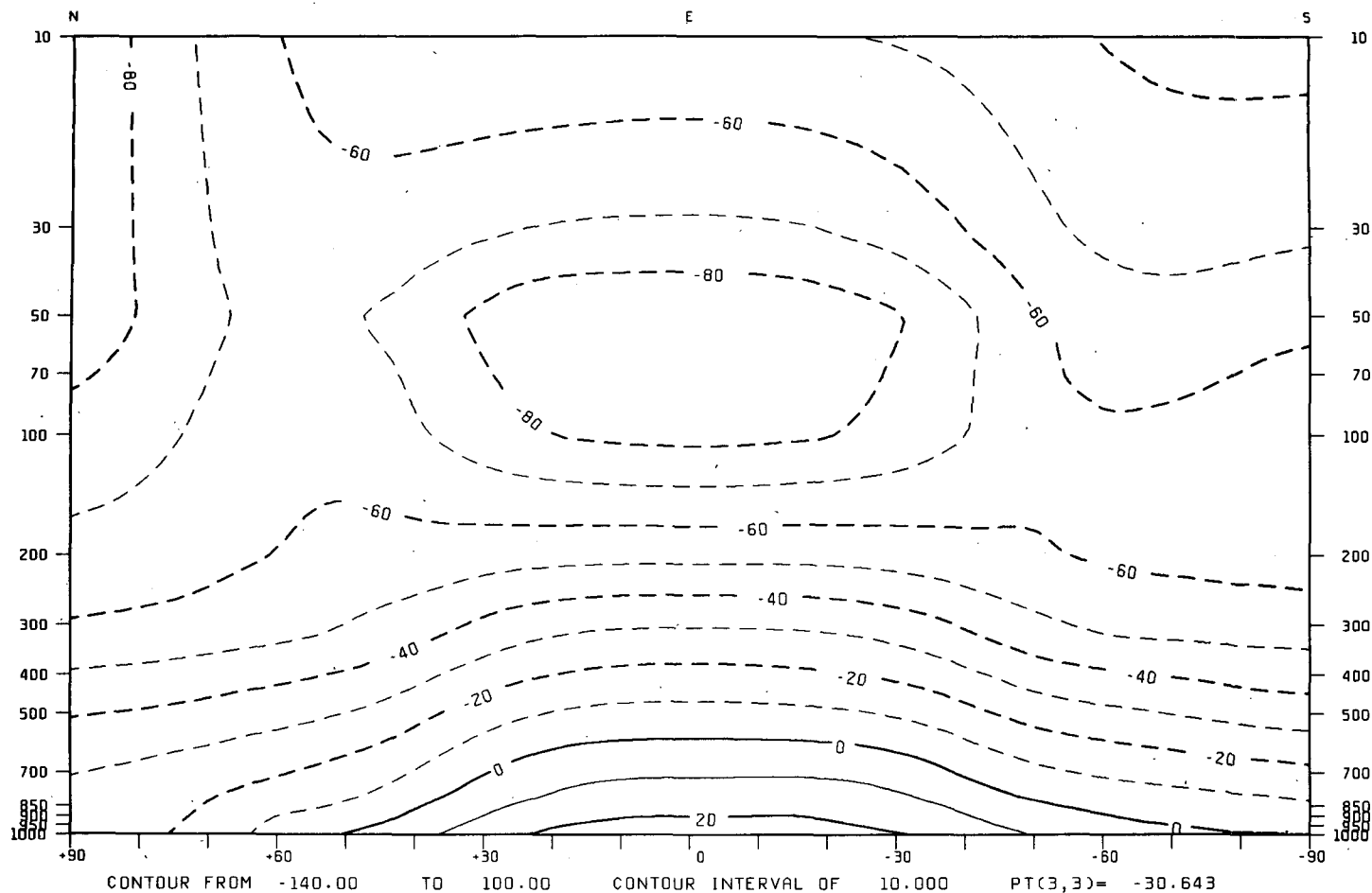


FIG. 9. As in Fig. 7, except for WD.

Since a GCM such as the one used here is designed to be used primarily for simulating the tropospheric circulation some lack of realism in representation of the stratospheric part of the circulation may be tolerable provided there are not significant corresponding defects in the simulated tropospheric circulation. In this regard it has been noted that in the wave drag experiment the simulated zonally averaged westerly flow in the troposphere is much more realistic than that of the control experiment.

*b. Mean sea level pressure and geopotential height fields*

The time averaged mean sea level pressure field generated in the control simulation is shown in Fig. 14, while that for the wave drag experiments is shown in Fig. 15. The observed climatological field for January is displayed in Fig. 16.

The most obvious differences between the control and wave drag simulations are found in middle and

high latitudes in the Northern Hemisphere. Although both of the simulations do reproduce the main features of climatological pressure patterns, the control simulation shows a bias toward excessive development of the Aleutian and Icelandic low-pressure regions with an associated underdevelopment of the high-pressure ridge over western North America. Figure 15 shows that this bias is not present in the wave drag simulations. The mean sea level pressure field for this simulation is more similar to midseason climatology (Fig. 16).

In the Northern Hemisphere middle and high-latitude mean sea level pressure patterns show a considerable amount of interannual variability, both in nature and in model simulations. This must be borne in mind when comparing single realizations of a seasonal simulation with a midseason climatological field. However, a number of additional numerical experiments have verified that without the wave drag parameterization the previously noted low-pressure bias is consistently

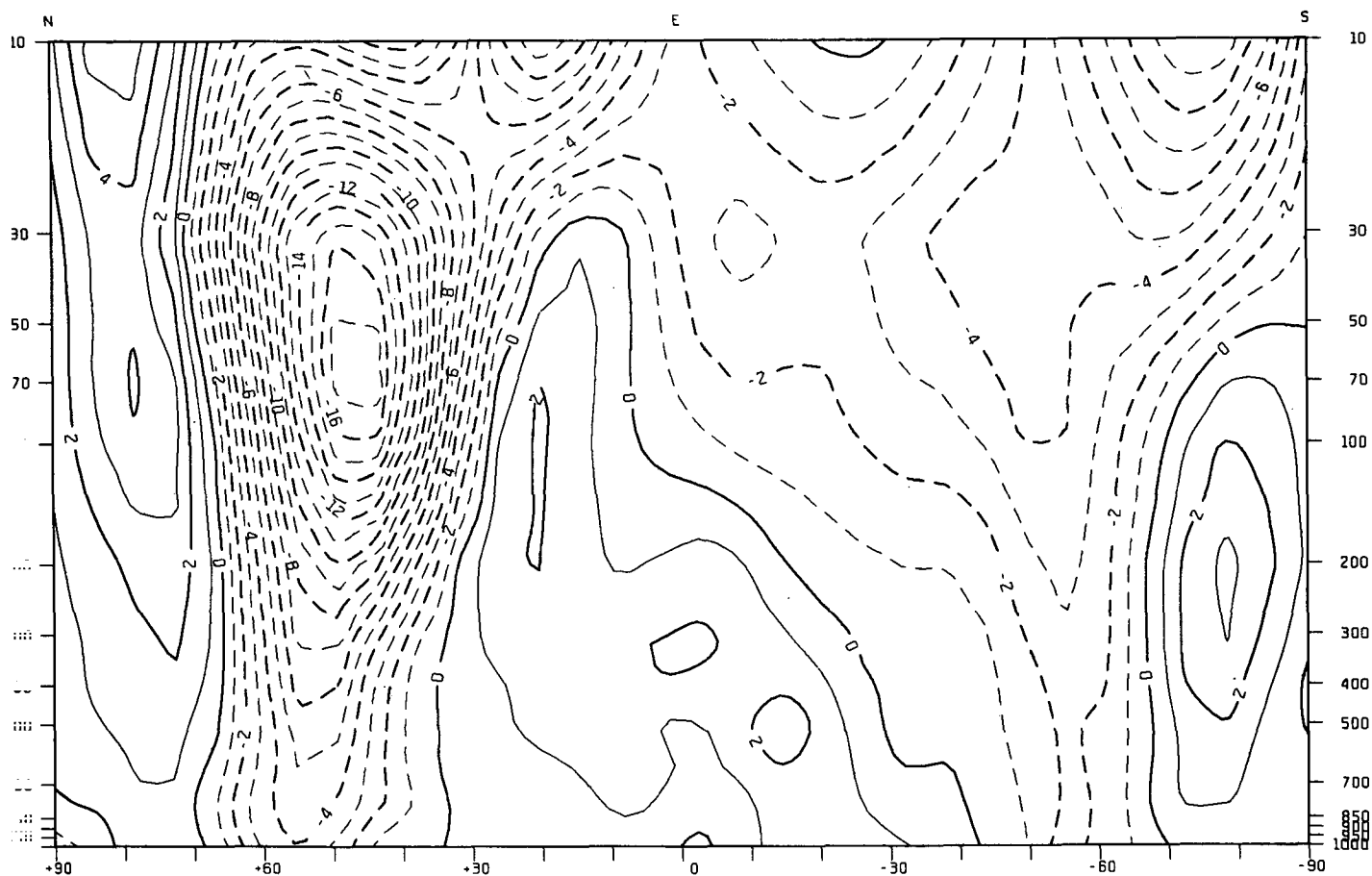


FIG. 10. Mean zonal flow difference (WD-CONTROL). Contours are  $1 \text{ m s}^{-1}$ .

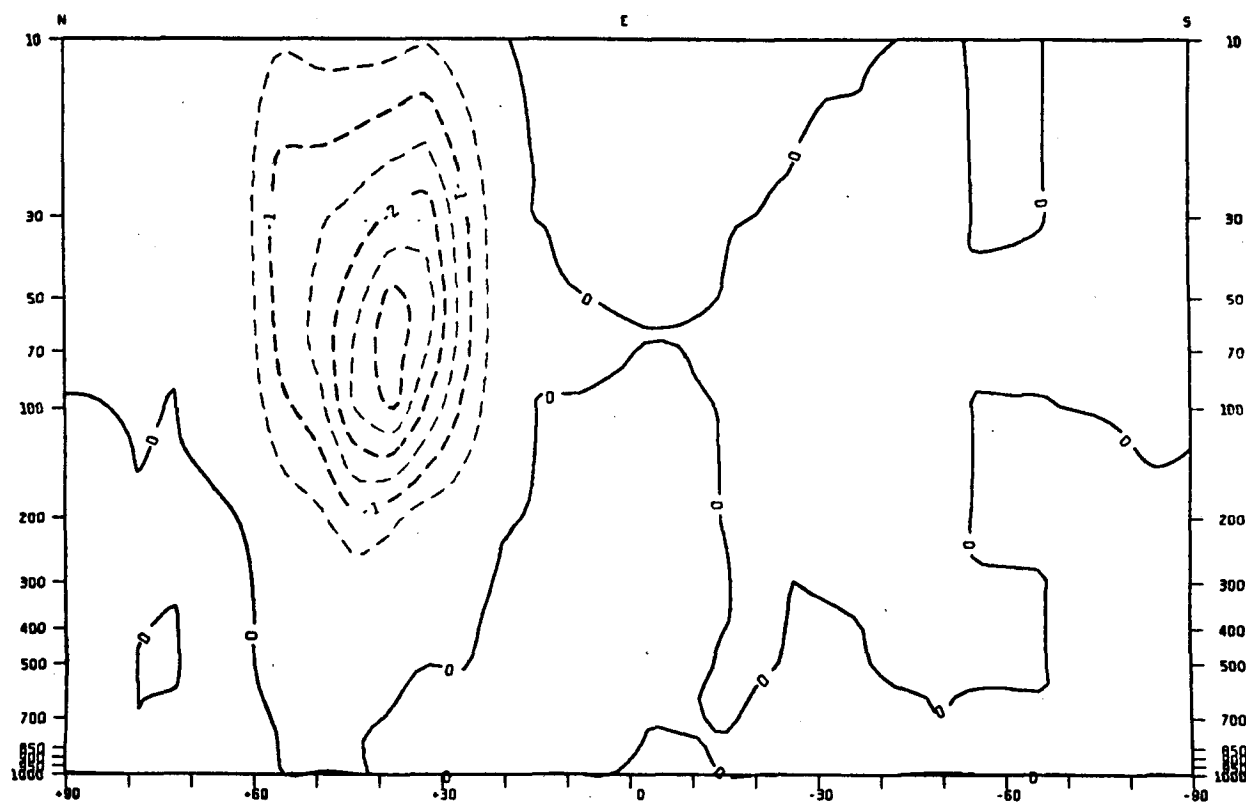


FIG. 11. Zonally averaged westerly wind deceleration due to wave drag.

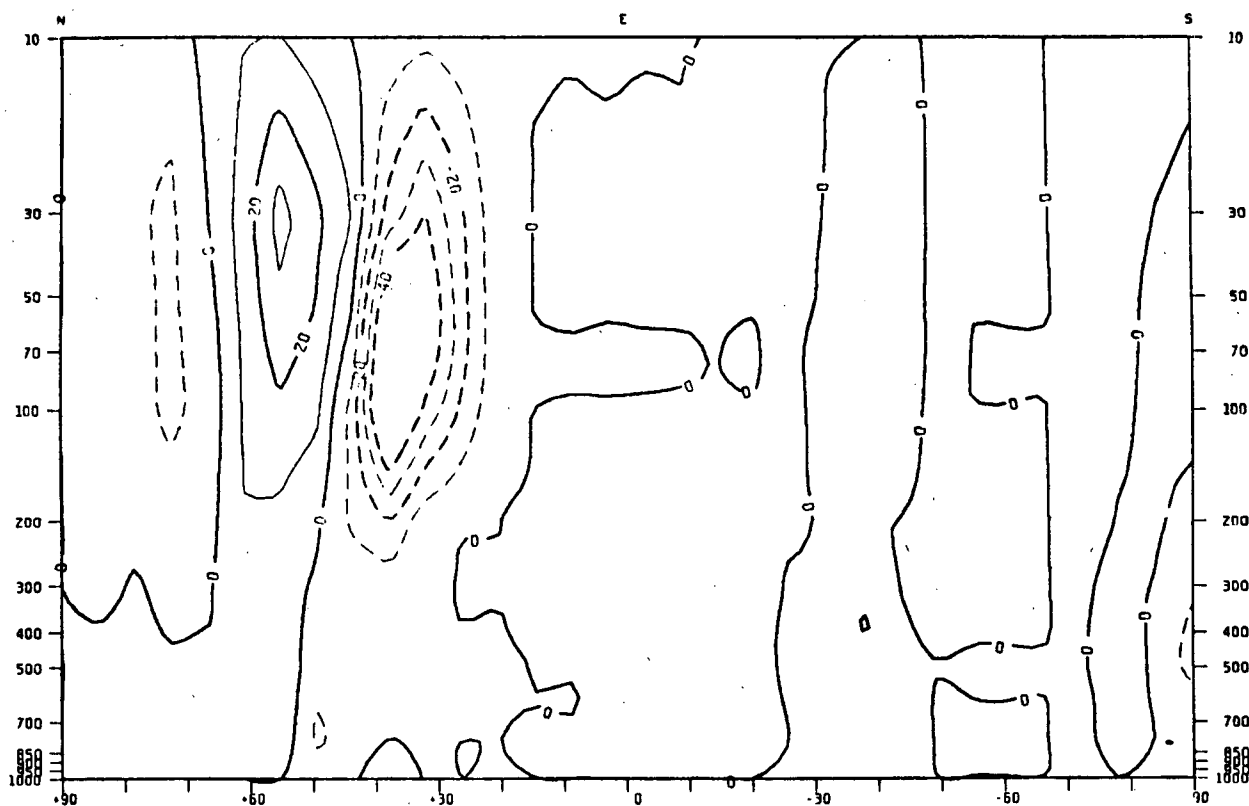


FIG. 12. As in Figure 11, except for the meridional flow. Values shown have been multiplied by a factor of 100.

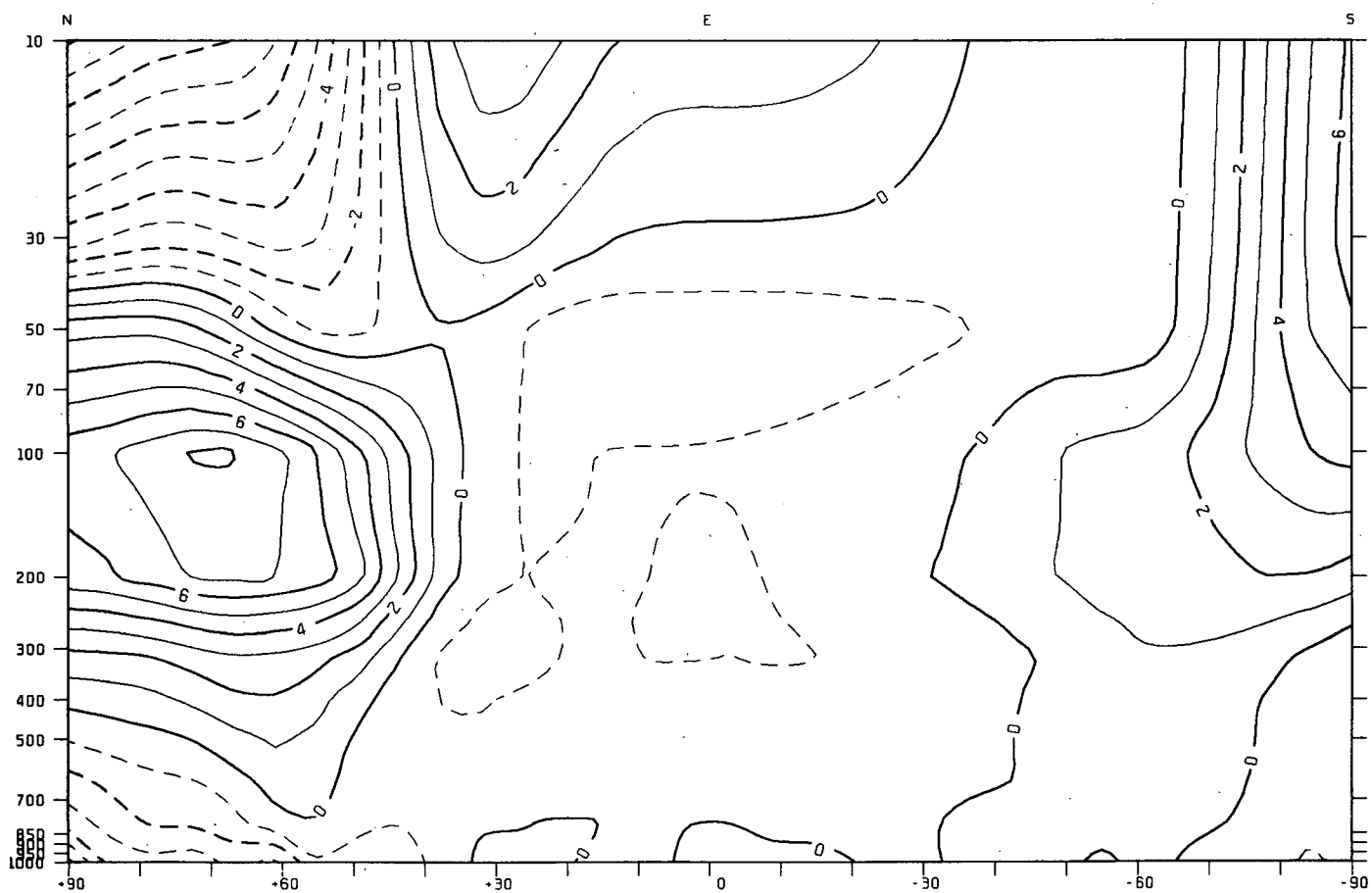


FIG. 13. Zonal mean temperature difference (WD-CONTROL). Units: degrees K.



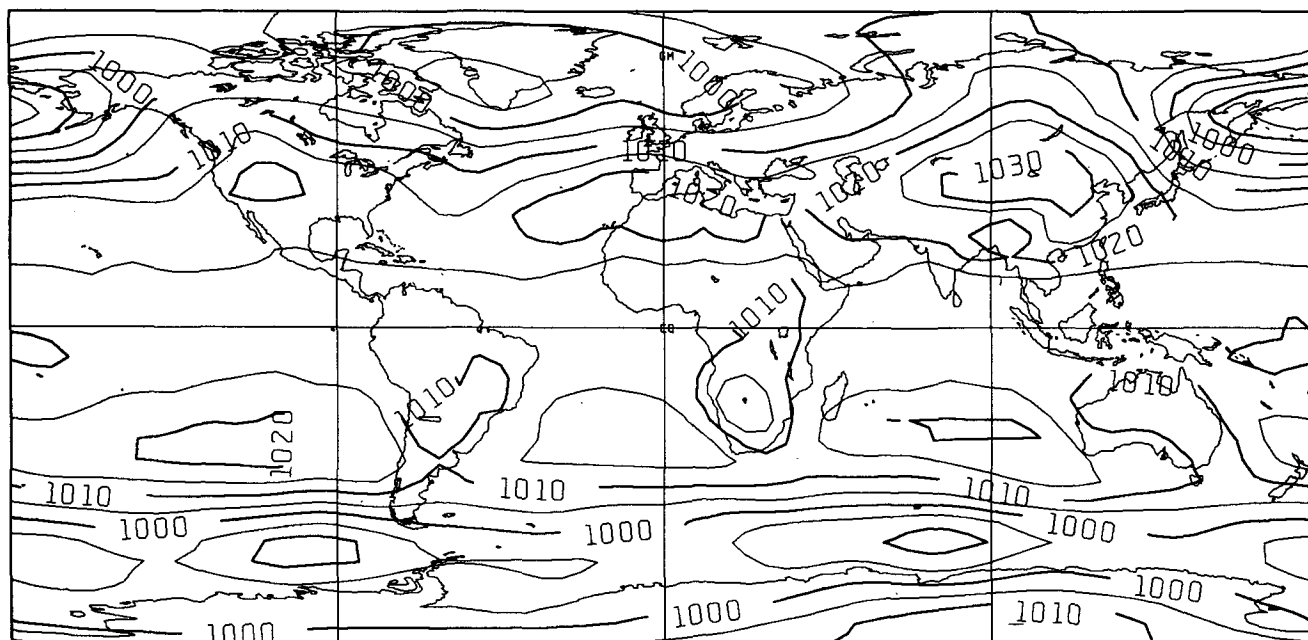


FIG. 14. Time averaged mean sea level pressure for the control simulation. Contour interval 5 mb.

present. As mentioned in the introductory remarks, other large-scale primitive equations models have similar biases.

The foregoing remarks apply also to simulations of tropospheric geopotential height fields. This is illustrated for 500 mb geopotential height fields in Figs. 17 and 18. Again, the climatological high-pressure ridges

over western North America and the eastern Atlantic Ocean are present but less developed in the control rather than the wave drag simulation. In this respect, also, the wave drag simulation is in better accord with the observed climatology.

The impact of the wave drag parameterization on the surface pressure and geopotential height fields can

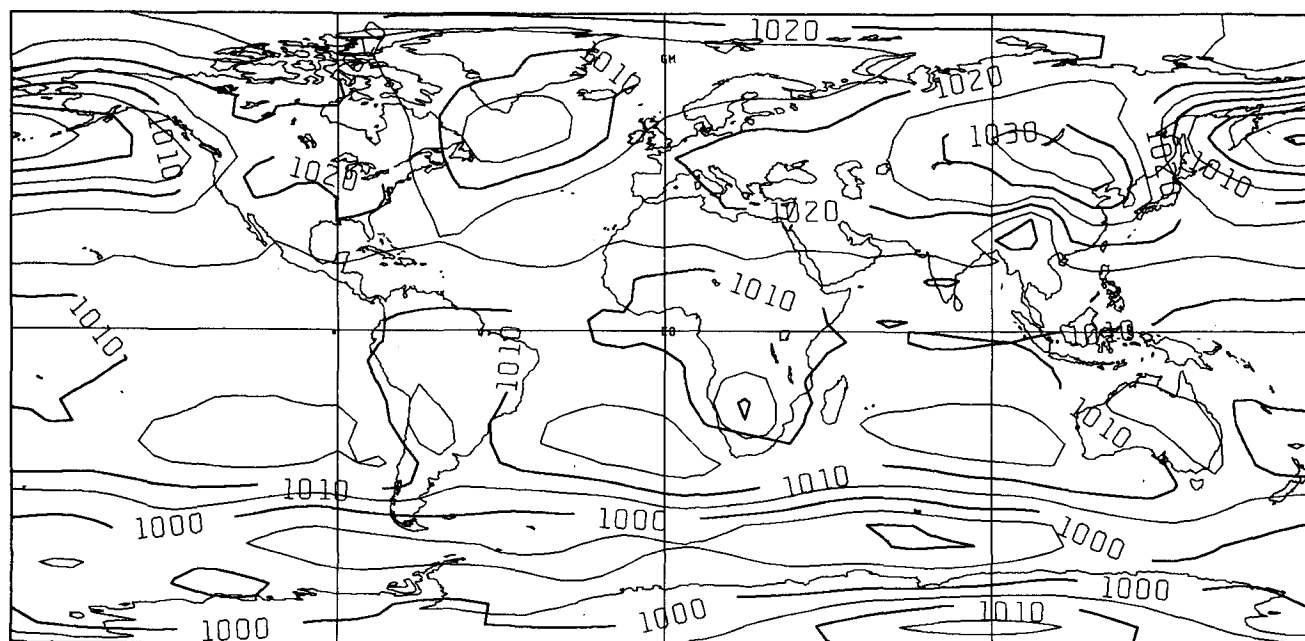


FIG. 15. As in Figure 14, except for WD.

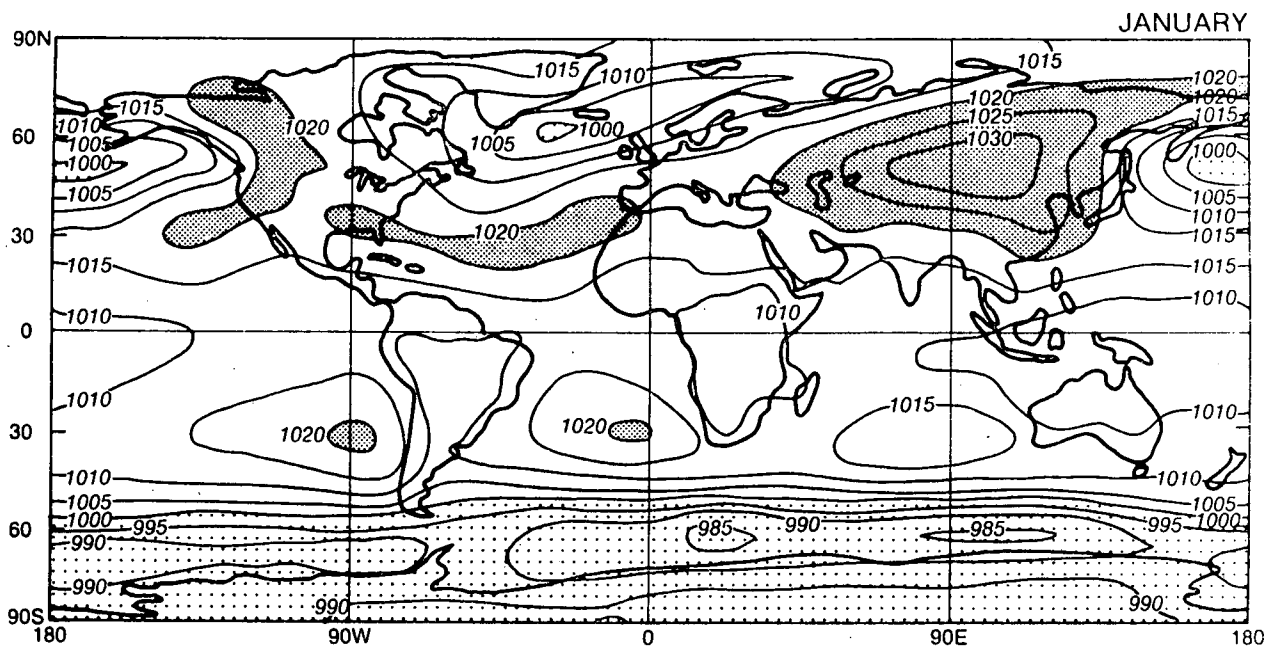


FIG. 16. Observed climatological mean sea level pressure for January. (After Taljaard et al., 1969, and Crutcher and Meserve, 1970).

be seen quite clearly in Figs. 19 and 20. The first of these shows the difference between mean sea level pressure fields for the two experiments while the second depicts the 500 mb geopotential height field difference. These figures show that higher geopotential heights in the Northern Hemisphere polar regions are found in the wave drag experiment in association with higher surface pressures.

Most of the foregoing discussion has focused on simulation of the Northern Hemisphere winter climate. Inspection of the figures which have been presented shows that the wave drag parameterizations have had much less impact in the Southern Hemisphere. This has been found to be true in all seasons. In part this is because the region of strongest tropospheric flow in middle latitudes is predominantly over oceanic regions.

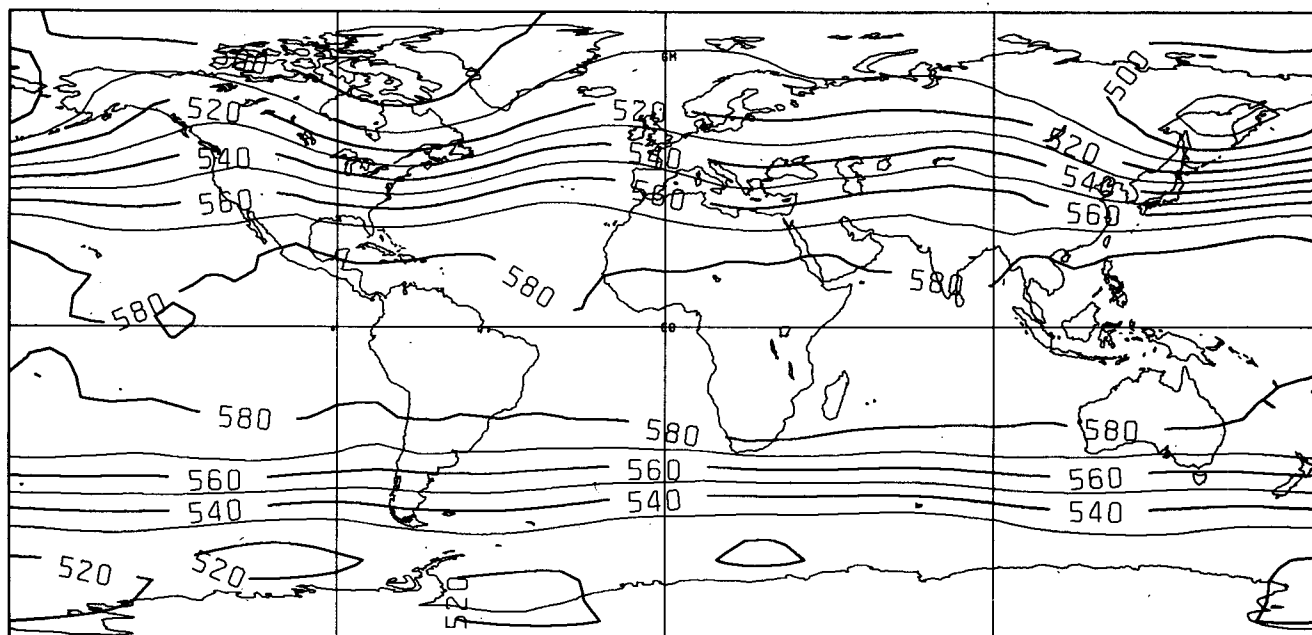


FIG. 17. Time averaged 500 mb geopotential height field for the control simulation.

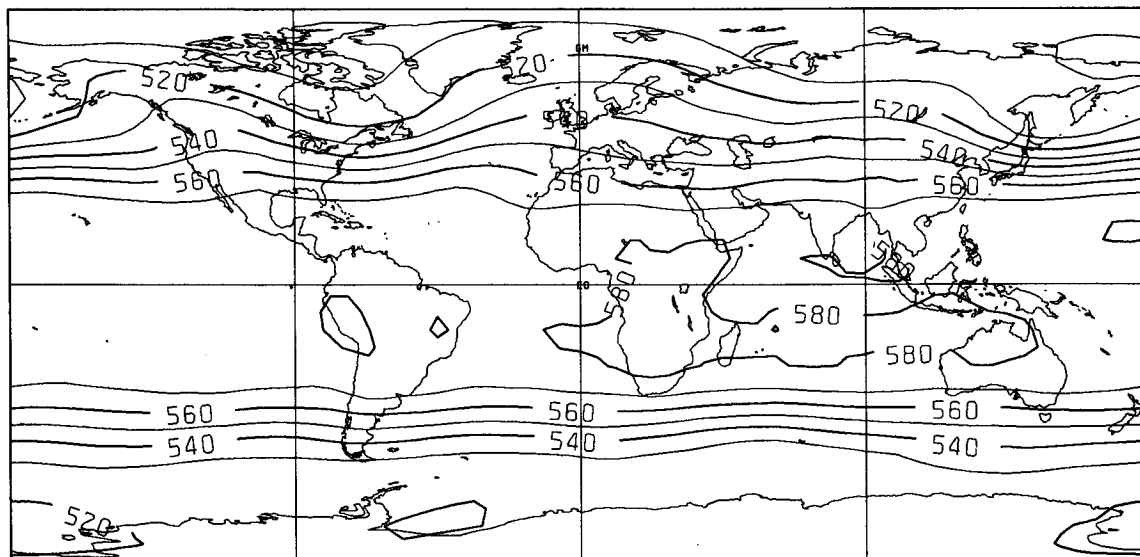


FIG. 18. As in Figure 16, except for WD.

The flow is generally weaker and more variable with height, both in speed and direction, over continental regions where there is substantial subgrid-scale orographic variance. Thus, wave drag effects are weaker and/or confined to the lower troposphere where they may be largely masked by the effects of boundary layer turbulence.

For essentially the same reason (weak winds in the troposphere) it has been found that wave drag effects are much less pronounced in simulations of the Northern Hemisphere summer climate. For instance, it has been found that simulations of mean sea level pressure and tropospheric geopotential height fields in the Northern Hemisphere summer season are not substantially affected by the wave drag parameterization.

#### c. Horizontal variation of wave drag effects

Figure 21 depicts the horizontal structure of the magnitude of the vertically integrated wave drag force expressed in units of surface stress (Pa). Relatively large values are, as expected, found over mountainous regions of the globe. Over the Rocky Mountains, for example, values range between 0.05 and 0.3 Pa. Although the upper limit is somewhat larger than the mean value observed by Lilly et al. (1982) it is well within the range of observed values.

It is interesting to note that in the Southern Hemisphere most of the wave drag occurs over the highest parts of the Andes Mountains where values are generally less than 0.2 Pa. The narrow longitudinal extent of this region and the relative weakness of the wave drag effects explain the absence of a substantial and widespread response in the Southern Hemisphere.

Figure 22 shows the zonal mean of the magnitude of the net momentum flux divergence depicted in Fig.

21. As mentioned before, some wave energy may escape through the top of the model. Figure 23 shows the zonal-averaged magnitude of that part of the wave momentum flux which escapes. Comparing this figure with the previous one readily shows that most of the wave energy is depleted within the domain of the model.

#### d. Sensitivity to vertical resolution

The fact that the wave drag force is largest and most extensive in the lower stratosphere raises a question as to whether the effects obtained in the wave drag experiment may be sensitive to vertical resolution in that region. To examine this question experiment WDH was performed. This experiment was identical to WD except that the vertical resolution between the model levels at  $\sigma = 0.032$  and  $\sigma = 0.360$  (see Table 1) was doubled.

Figure 24 shows the zonally averaged westerly wind structure obtained in this experiment. Although some differences between this simulation and WD are apparent, the two are broadly similar. An obvious difference is that the tropospheric jet maximum in the Northern Hemisphere is slightly larger in magnitude in the higher resolution experiment. This may be due in part to the fact that this feature is better resolved.

The mean sea level pressure and geopotential height fields (not shown) are also broadly similar to those for the lower resolution wave drag experiment. Thus the vertical resolution used for the WD experiment is adequate to capture the salient features of the wave drag effect.

### 5. Discussion

It has been demonstrated that, despite its simplicity, the wave drag parameterization proposed in section 2

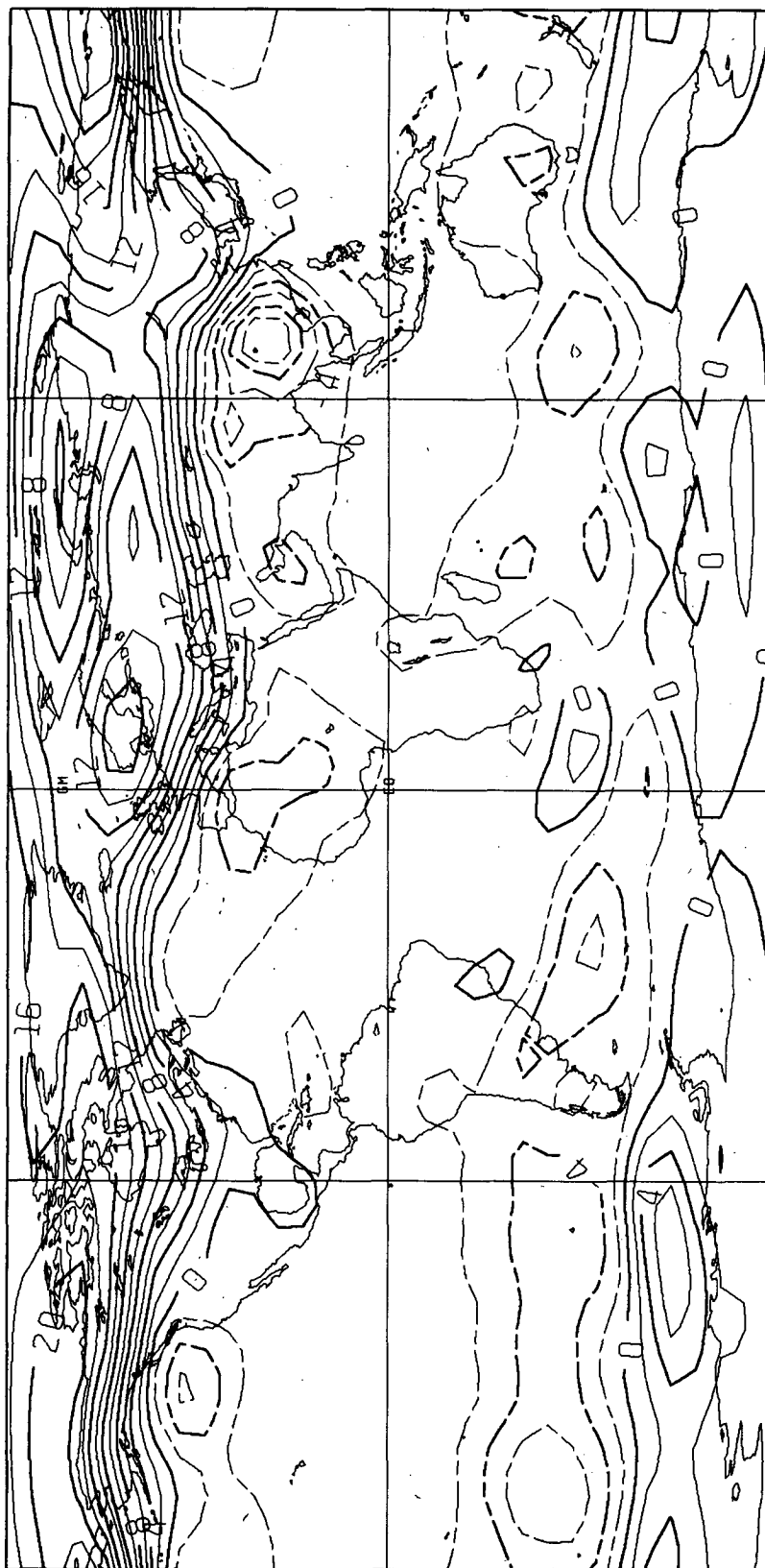


FIG. 19. Mean sea level pressure difference (WD-CONTROL). Contour interval: 2 mb.

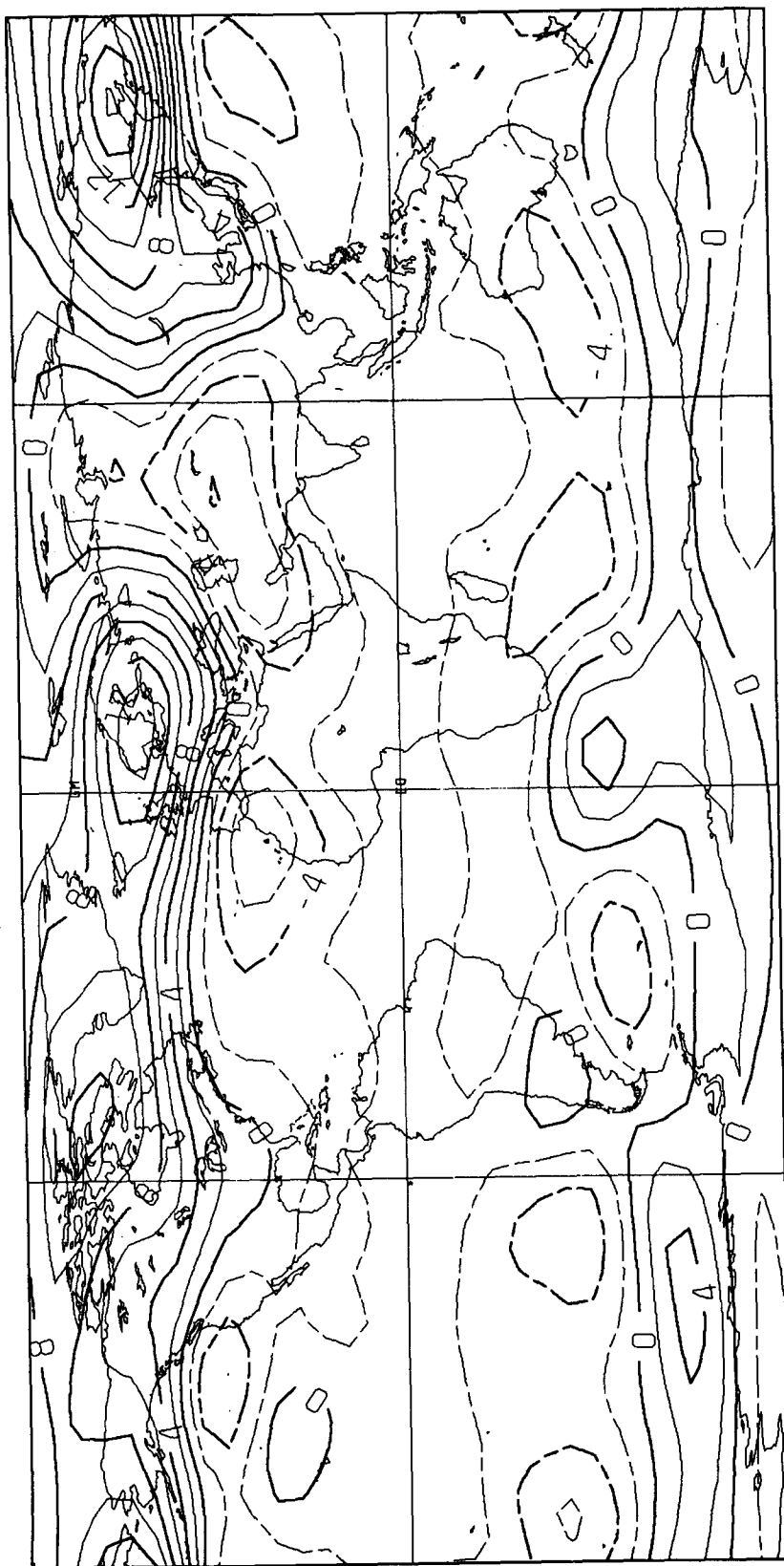


FIG. 20. 500 mb geopotential difference (WD-CONTROL). Contour interval: 200 (m s<sup>-1</sup>)<sup>2</sup>.

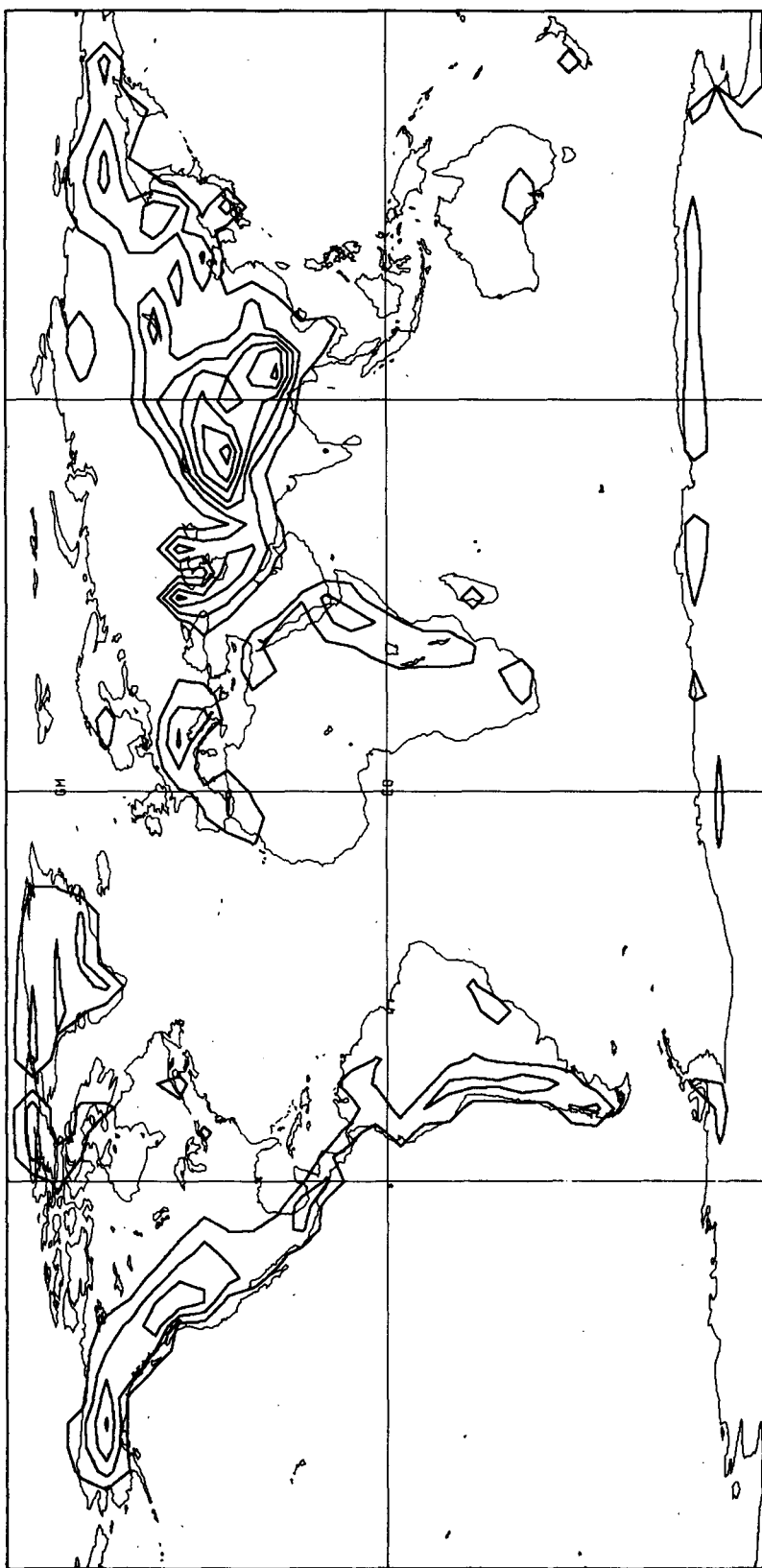


FIG. 21. Net stress drop over the vertical model domain due to the wave drag force. Contours are for 0.05 Pa and larger with an interval of 0.1 Pa.

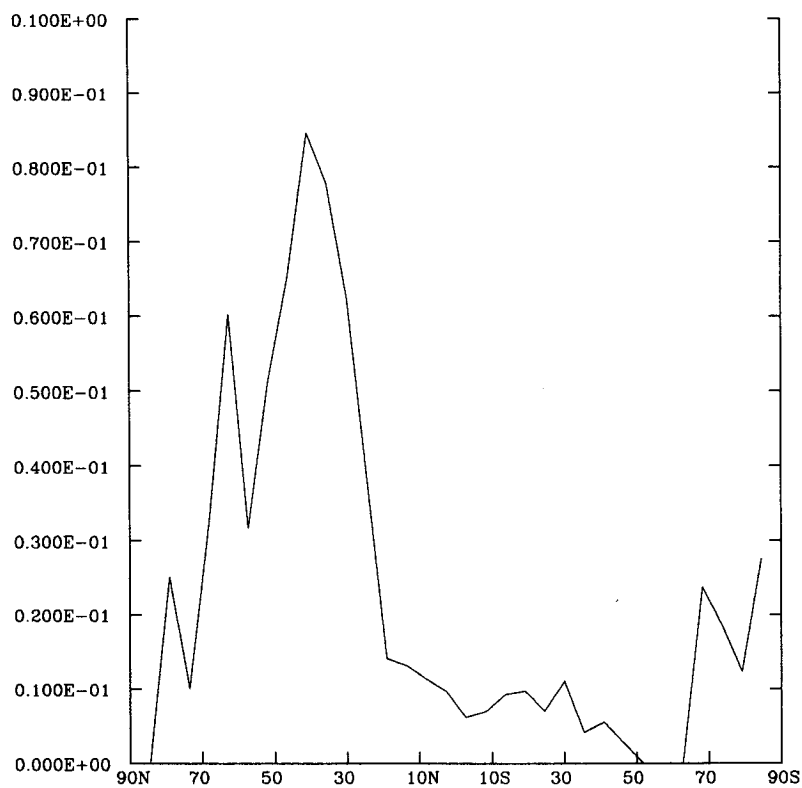


FIG. 22. As in Fig. 21 except zonally averaged. Units: pascals.

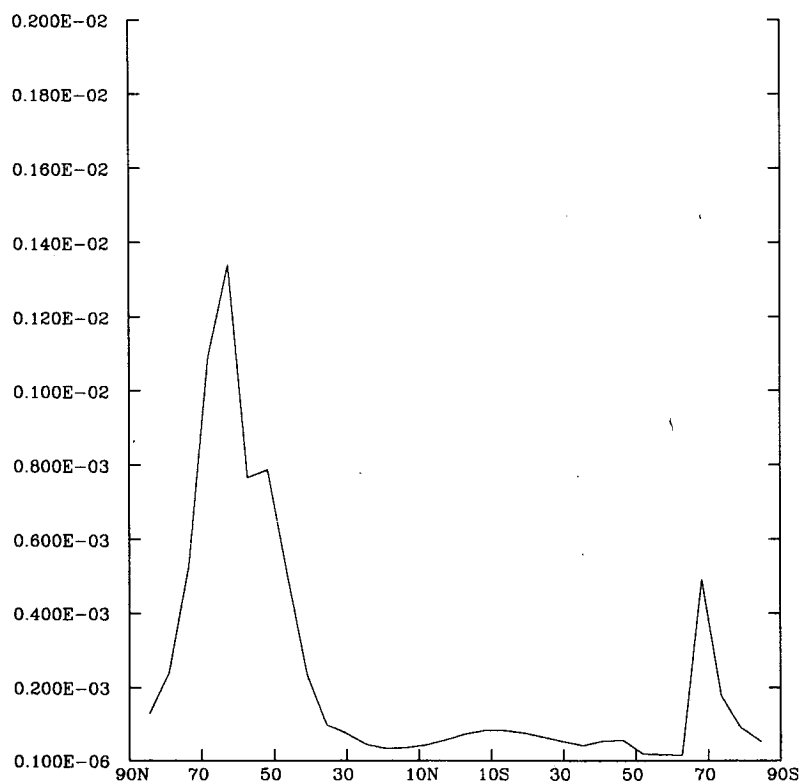


FIG. 23. Wave momentum flux which escapes through the top of the model. Units: pascals.

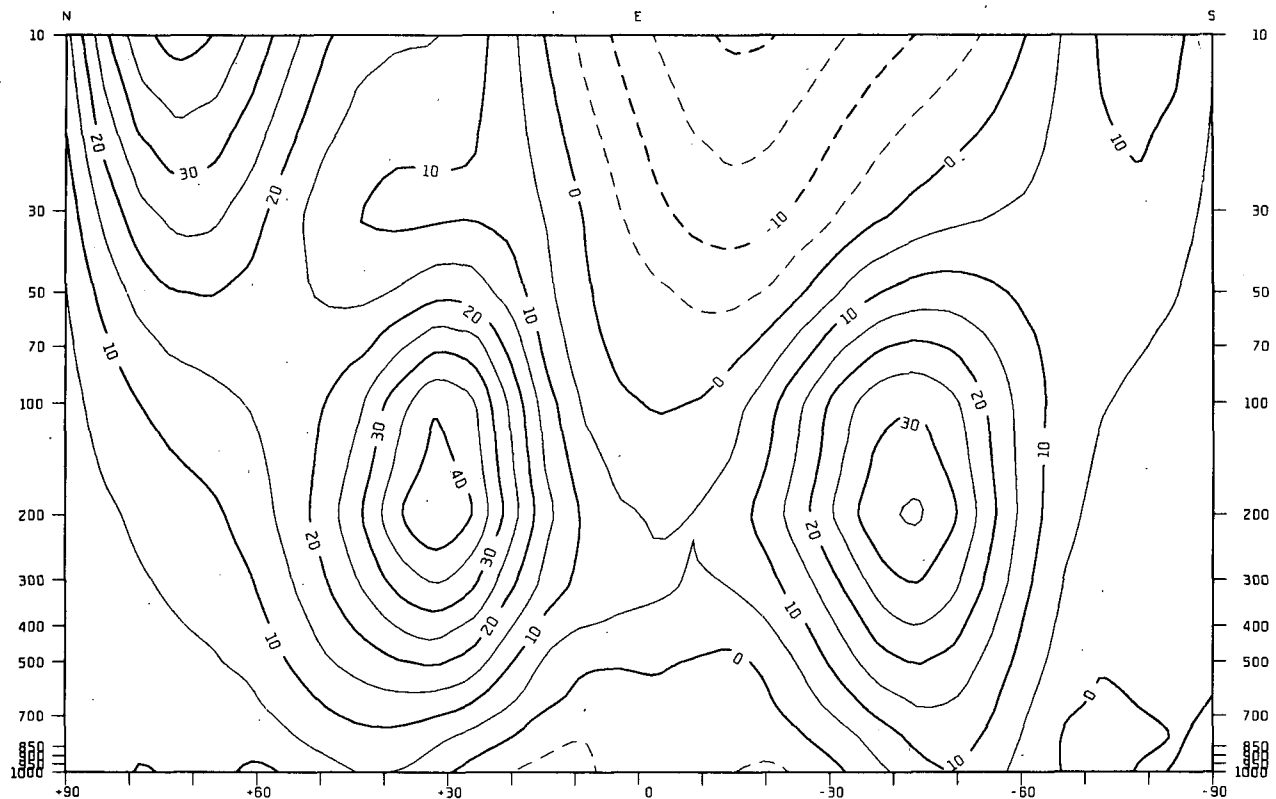


FIG. 24. Mean zonal winds for the experiment WDH.

has a generally beneficial impact on GCM climate simulations. To some extent the results suggest that, for climate simulations at least, the most important wave drag effects can be captured with a highly simplified parameterization.

Palmer et al. (1985) have independently developed and tested an orographic wave drag parameterization in the British Meteorological Office general circulation model. They use a representation of the wave drag force which is similar to that employed here except that their critical Froude number ( $F_c$ ) is a function of the local gradient Richardson number associated with the large-scale flow. This accounts approximately for wave dissipation associated with the onset of both shear flow instability and convective instability. They also assume vanishing of the wave momentum flux at the top of the model in the absence of a critical line within the resolved vertical domain.

They show that this wave drag parameterization has an impact on the GCM climatology which is similar to that found in the experiments discussed in the present paper. They also show, using a simple analytical zonal mean model, how the impacts on the zonal mean wind and temperature fields come about as dynamical consequences of the wave drag force.

Although the parameterization employed here demonstrates the importance of accounting for wave drag

processes in large-scale models, it is clearly oversimplified. Future work must address the problem of accounting more carefully for effects of processes which have been either neglected or misrepresented. These numerous and practical considerations dictate that a limited number of the more important ones should receive attention. This choice must be made on the basis of recent and ongoing theoretical and observational work.

Some of the neglected effects (for instance, those due to variations in orographic orientation) could be at least partially accounted for with relative ease. Others involve more fundamental questions concerning the gravity wave dynamics and therefore require careful consideration. For instance, the fact that nonlinearity enhances wave steepening in vertically localized regions while suppressing it elsewhere has a number of implications for the wave saturation process. More localized convective overturning would presumably cause the wave momentum flux profile to take on a steplike character with regions of maximum divergence being separated, approximately by distances of the order of a vertical wavelength. Bearing in mind the coarseness of the vertical resolution employed in most large-scale models it is not clear that replacing such a profile with a broader and smoother one seriously distorts the net response to the wave drag force.



A related and more important question concerns the effects of wave reflection in association with convective overturning. The previously cited work of Peltier and Clark (1979) indicates that turbulent dissipation alone may be insufficient to accomplish static stabilization without some downward reflection of excess wave energy. The wave amplification process discovered by these authors appears to be due to resonant growth resulting from constructive interference between upward and downward propagating components of the wave in the cavity formed between the surface and the lowest region of convective overturning.

More recently reported work by Clark and Peltier (1984) reinforces this conjecture by demonstrating that the occurrence of wave amplification when there is a critical level in the mean flow is confined to circumstances in which the region between critical level (which is the site of maximum convective instability) and the surface forms a resonant cavity.

The relevance of this process in the atmosphere is suggested by some of the documented features of strong wave events such as those studied by Lilly and Zipser (1972), Lilly (1978) and more recently by Hoinka (1985). Bearing in mind the resonant tuning requirement, it is possible that wave amplification occurs rather sporadically and may also sometimes be inhibited by other effects such as those due to the occurrence of latent heat release (Durrant and Klemp, 1983). Although the available observational data would tend to support this conjecture they are too sparse and uncertain to permit much confidence in such an assertion. Thus some importance must be attached to the problem of accounting for the effects of this process in future wave drag parameterizations. Although Peltier and Clark (1979) have gone a long way toward delineating its salient features there is still a number of uncertainties concerning the basic dynamics involved.

There are, of course, numerous other potentially important effects which future work must take into account. Much of the recent and ongoing theoretical work in this area is concerned with unravelling the complexities of gravity wave propagation and saturation processes. Strong motivation for such work comes from the accumulating evidence of the important role of these processes in the dynamics of the large-scale circulation in both the lower and middle atmosphere.

**Acknowledgments.** Dr. Clément Chouinard prepared the orographic height variance field used in this study and Mr. René Laprise provided a great deal of help in implementing the wave drag scheme in the GCM. Lynda Smith typed the manuscript and John Strechan-sky drafted the figures. The help of all is acknowledged with gratitude. It is also a pleasure to thank Dr. George Boer and Dr. Kevin Hamilton for reading the manuscript and suggesting improvements. The author also wishes to thank Dr. T. Palmer and another anonymous

reviewer for comments which led to improvement of the paper.

## APPENDIX

### Numerical Treatment

The wave drag force, in the normalized pressure coordinate system, may be written as follows:

$$(\partial \mathbf{V} / \partial t) g = -\mathbf{n} \partial (MU) / \partial \sigma \quad (\text{A1})$$

where  $\mathbf{n}$  is a unit vector parallel to the reference level flow and  $U$  is the component of the local flow which is parallel to that flow. The quantity  $M$  is defined as follows:

$$M = \alpha \sigma N A^2 / H \quad (\text{A2})$$

where  $H$  is the local density scale height and  $\alpha$  is used to denote the quantity  $(E \mu e / 2)$  as specified in section 3.

The wave amplitude,  $A$ , is such that the product  $(MU)$  is independent of  $\sigma$  except in wave saturation regions where  $A$  is chosen such that the quantity  $AN / (F_c U)$  is unity. Hence, in those regions

$$M = \alpha \sigma F_c^2 U^2 / (NH). \quad (\text{A3})$$

The numerical treatment makes use of the following relationships:

$$(\partial \mathbf{V} / \partial t) g = \mathbf{n} \partial U / \partial t \quad (\text{A4})$$

$$\partial U / \partial t = -\partial (MU) / \partial \sigma. \quad (\text{A5})$$

Defining

$$(\delta U / \delta t) = [U(t + \Delta) - U(t)] / \Delta,$$

Equation A5 is written in finite difference form as follows:

$$\begin{aligned} (\delta \sigma)_j (\delta U / \delta t)_j &= -\frac{1}{2} \left\{ (MU)_{j+1} + (MU)_j + \left[ \frac{\partial (MU)}{\partial U} \right]_j \left( \frac{\delta U}{\delta t} \right)_j \Delta \right\} \\ &+ \frac{1}{2} \left\{ (MU)_j + (MU)_{j-1} + \left[ \frac{\partial (MU)}{\partial U} \right]_{j-1} \left( \frac{\delta U}{\delta t} \right)_{j-1} \Delta \right\} \end{aligned} \quad (\text{A6})$$

where the index  $(j)$  increases from the top downward. In wave saturation regions A3 implies that

$$\partial (MU) / \partial U = 3M. \quad (\text{A7})$$

Elsewhere  $(MU)$  is independent both of  $\sigma$  and  $U$ . Hence in (A6) the following formulation is used:

$$\left[ \frac{\partial (MU)}{\partial U} \right]_j = 3M_j \epsilon_j \quad (\text{A8})$$

with  $\epsilon_j$  being unity when  $(MU)_{j+1} > (MU)_j$  and zero otherwise.

Above the uppermost model level and below the reference level it is assumed that  $(MU)$  is constant and

( $\partial U/\partial t$ ) vanishes. The alternative condition that ( $MU$ ) vanishes at the top of the model poses no difficulty since this condition also implies vanishing of  $\partial(MU)/\partial U$ . In practice the reference level is at or above the interface between the two lowest model layers. Equation A6 is easily solved for ( $\delta U/\delta t$ ) at each level by starting from the uppermost level and working downward.

Although computational stability considerations are not really relevant here because both  $M$  and  $U$  are intrinsically positive, it is interesting to note that, viewed as a time stepping scheme, A6 and A8 are stable for all values of  $M$  and  $U$ . However, A6 is ill-conditioned for determination of ( $\delta U/\delta t$ ) if  $M$  is negative.

#### REFERENCES

- Boer, G. J., N. A. McFarlane, R. Laprise, J. D. Henderson and J.-P. Blanchet, 1984a: The Canadian Climate Centre spectral atmospheric General Circulation Model. *Atmosphere: Atmosphere-Ocean*, **22**, 397-429.
- , —, and —, 1984b: The climatology of the Canadian Climate Centre General Circulation Model as obtained from a five-year simulation. *Atmosphere: Atmosphere-Ocean*, **22**, 430-473.
- Booker, J. R., and F. P. Bretherton, 1967: The critical layer for internal gravity waves in a shear flow. *J. Fluid Mech.*, **27**, 513-539.
- Boville, B. A., 1984: Influence of the Polar Night Jet on the tropospheric circulation in a GCM. *J. Atmos. Sci.*, **41**, 1132-1142.
- Brown, P. R. A., 1983: Aircraft measurements of mountain waves and their associated momentum flux over the British Isles. *Quart. J. Roy. Meteor. Soc.*, **109**, 849-865.
- Clark, T. L., and W. R. Peltier, 1984: Critical level reflection and the resonant growth of nonlinear mountain waves. *J. Atmos. Sci.*, **41**, 3122-3134.
- Crutcher, H. L., and J. M. Meserve, 1970: Selected level heights, temperatures, and dew points for the Northern Hemisphere. NAVAIR 50-1C-52, Naval Weather Service Command, Washington, DC.
- Durran, D. R., and J. B. Klemp, 1983: A compressible model for the simulation of moist mountain waves. *Mon. Wea. Rev.*, **111**, 2341-2361.
- Fritts, D. C., 1984: Gravity wave saturation in the middle atmosphere: A review of theory and observations. *Rev. Geophys. and Space Phys.*, **22**, 275-308.
- Hoinka, K. P., 1985: Observations of the air flow over the Alps during a Föhn event. *Quart. J. Roy. Meteor. Soc.*, **111**, 199-224.
- Holton, J. R., 1982: The role of gravity wave-induced drag and diffusion in the momentum budget of the mesosphere. *J. Atmos. Sci.*, **39**, 791-799.
- Klemp, J. B., and D. K. Lilly, 1975: The dynamics of wave-induced downslope winds. *J. Atmos. Sci.*, **32**, 320-339.
- Lilly, D. K., 1972: Wave momentum flux: A GARP problem. *Bull. Amer. Meteor. Soc.*, **20**, 17.
- , 1978: A severe downslope wind storm and aircraft turbulence event induced by a mountain wave. *J. Atmos. Sci.*, **35**, 59-77.
- , and P. J. Kennedy, 1973: Observations of a stationary mountain wave and its associated momentum flux and energy dissipation. *J. Atmos. Sci.*, **30**, 1135.
- , and J. B. Klemp, 1979: The effects of terrain shape on nonlinear hydrostatic mountain waves. *J. Fluid Mech.*, **95**, 241-261.
- , and E. J. Zipser, 1972: The front range windstorm of 11 January 1972—A meteorological narrative. *Weatherwise*, **25**, 56-63.
- , J. M. Nicholls, R.-M. Chervin, P. J. Kennedy and J. B. Klemp, 1982: Aircraft measurements of wave momentum flux over the Colorado Rocky Mountains. *Quart. J. Roy. Meteor. Soc.*, **108**, 625-642.
- Lindzen, R. S., 1981: Turbulence and stress owing to gravity wave and tidal breakdown. *J. Geophys. Res.*, **86**, 9707-9714.
- , and J. Forbes, 1983: Turbulence originating from convectively stable internal waves. *J. Geophys. Res.*, **88**, 6549.
- Machenhauer, B., and E. Rasmussen, 1972: On the integration of the spectral hydrodynamical equations by a transform method. Rep. No. 3, Institut for Teoretisk Meteorologi, Kobenhavns Universitet, Denmark, 44 pp.
- Mahlman, J. D., and L. J. Umscheid, 1984: Dynamics of the middle atmosphere: Successes and problems of the GFDL "SKYHI" General Circulation Model. *Dynamics of the Middle Atmosphere*, J. R. Holton and T. Matsuno, Eds., Terra Scientific, 501-525.
- Newell, R. E., J. W. Kidson, D. G. Vincent and G. J. Boer, 1972: *The General Circulation of the Tropical Atmosphere and Interactions with Extratropical Latitudes*. Vol. 1, The MIT Press, 258 pp.
- , —, —, and —, 1974: *The General Circulation of the Tropical Atmosphere and Interactions with Extratropical Latitudes*. Vol. 2, The MIT Press, 371 pp.
- Ogura, Y., and N. A. Phillips, 1962: Scale analysis of deep and shallow convection in the atmosphere. *J. Atmos. Sci.*, **19**, 173-179.
- Orzag, S. A., 1970: Transform method for the calculation of vector-coupled sums: Application to the spectral form of the vorticity equation. *J. Atmos. Sci.*, **27**, 890-895.
- Palmer, T. N., G. J. Shutts and R. Swinbank, 1985: Alleviation of a systematic westerly bias in general circulation and numerical weather prediction models through an orographic gravity drag parameterization. To be submitted to the *Quart. J. Roy. Meteor. Soc.*
- Peltier, W. R., and T. L. Clark, 1979: The evolution and stability of finite-amplitude mountain waves. Part II: Surface wave drag and severe downslope windstorms. *J. Atmos. Sci.*, **36**, 1498-1529.
- , and —, 1983: Nonlinear mountain waves in two and three spatial dimensions. *Quart. J. Roy. Meteor. Soc.*, **109**, 527-548.
- Phillips, N. A., 1957: A coordinate system having some special advantages for numerical forecasting. *J. Meteor.*, **14**, 184-185.
- Ramanathan, V., E. J. Pitcher, R. C. Malone and M. L. Blackmon, 1983: The response of a spectral general circulation model to refinements in radiative processes. *J. Atmos. Sci.*, **40**, 605-630.
- Smith, R. B., 1977: The steepening of hydrostatic mountain waves. *J. Atmos. Sci.*, **34**, 1634-1654.
- Snyder, W. H., R. S. Thompson, R. E. Eskridge, R. E. Lawson, I. P. Castro, J. T. Lee, J. R. C. Hunt and Y. Ogawa, 1985: The structure of strongly stratified flow over hills: Dividing-streamline concept. *J. Fluid Mech.*, **152**, 249-288.
- Taljaard, J. J., H. van Loon, H. L. Crutcher and R. L. Jenne, 1969: Climate of the upper air: Southern Hemisphere. Vol. 1. Temperatures, dew points and heights at selected pressure levels. NAVAIR 50-1C-55.
- Wallace, J., S. Tibaldi and A. Simmons, 1983: Reduction of systematic forecast errors in the ECMWF model through the introduction of an envelope orography. *Quart. J. Roy. Meteor. Soc.*, **109**, 683-717.